

AD-A155 070

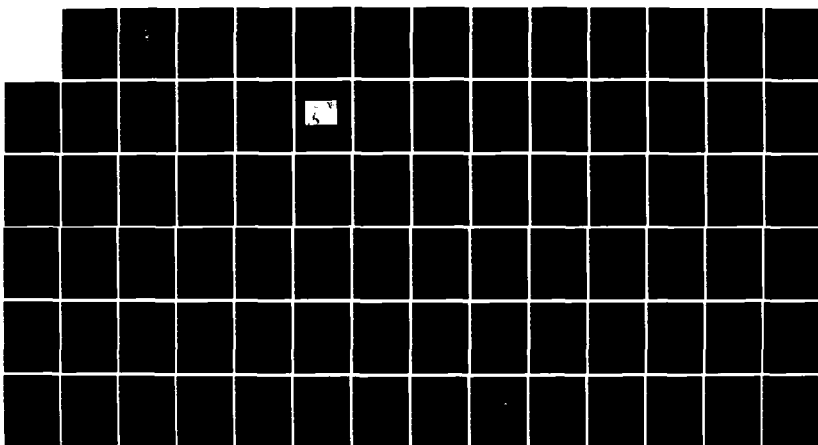
DESIGN OF A FREESTANDING NOISE MEASUREMENT AND
RECORDING SYSTEM TO PREDIC. (U) NAVAL POSTGRADUATE
SCHOOL MONTEREY CA M V ROSS DEC 84

1/1

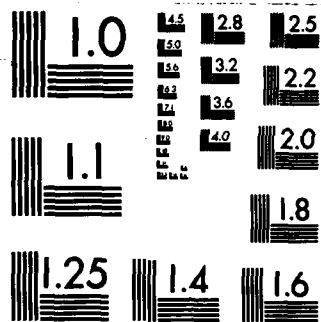
UNCLASSIFIED

F/G 8/11

NL



END
1/1



MICROCOPY RESOLUTION TEST CHART
NATIONAL BUREAU OF STANDARDS-1963-A

2

NAVAL POSTGRADUATE SCHOOL

Monterey, California

AD-A155 070



DTIC
ELECTE
JUN 14 1985
S B

THESIS

DESIGN OF A FREESTANDING NOISE MEASUREMENT
AND RECORDING SYSTEM TO PREDICT THE INTENSITY
AND LOCATION OF ELECTROMAGNETIC
RADIATION FROM EARTHQUAKES

by

Mickey V. Ross

December 1984

Thesis Advisor:

R. W. Adler

DTIC FILE COPY

Approved for public release; distribution unlimited

85 5 22 015

REPORT DOCUMENTATION PAGE		READ INSTRUCTIONS BEFORE COMPLETING FORM
1. REPORT NUMBER	2. GOVT ACCESSION NO. ADA155070	3. RECIPIENT'S CATALOG NUMBER
4. TITLE (and Subtitle) Design of a Freestanding Noise Measurement and Recording System to Predict the Intensity and Location of Electromagnetic Radiation from Earthquakes		5. TYPE OF REPORT & PERIOD COVERED Master's Thesis; December
7. AUTHOR(s) Mickey V. Ross		6. PERFORMING ORG. REPORT NUMBER
9. PERFORMING ORGANIZATION NAME AND ADDRESS Naval Postgraduate School Monterey, California 93943		8. CONTRACT OR GRANT NUMBER(s)
11. CONTROLLING OFFICE NAME AND ADDRESS Naval Postgraduate School Monterey, California 93943		10. PROGRAM ELEMENT, PROJECT, TASK AREA & WORK UNIT NUMBERS
14. MONITORING AGENCY NAME & ADDRESS (if different from Controlling Office)		12. REPORT DATE December 1984
		13. NUMBER OF PAGES 81
		15. SECURITY CLASS. (of this report) UNCLASSIFIED
		15a. DECLASSIFICATION/DOWNGRADING SCHEDULE
16. DISTRIBUTION STATEMENT (of this Report) Approved for public release; distribution unlimited		
17. DISTRIBUTION STATEMENT (of the abstract entered in Block 20, if different from Report)		
18. SUPPLEMENTARY NOTES		
19. KEY WORDS (Continue on reverse side if necessary and identify by block number) Noise Measurement; Prediction; Electromagnetic Radiation from Earthquakes		
20. ABSTRACT (Continue on reverse side if necessary and identify by block number) The design, construction, and testing of a freestanding radio frequency (RF) noise measurement and recording system in the 30 MHz and 150 MHz range is presented. Placement of the system along the San Andreas fault to permit the		

establishment of a correlation between increased background RF noise to earthquake fault activity for potential as an earthquake prediction tool is described.

Accession For	
NTIS GRA&I	<input checked="" type="checkbox"/>
DTIC TAB	<input type="checkbox"/>
Unannounced	<input type="checkbox"/>
Justification	
By	
Distribution/	
Availability Codes	
Dist	Avail and/or Special
A-1	

Approved for public release; distribution is unlimited.

Design of a Freestanding Noise Measurement and Recording System
to Predict the Intensity and Location of Electromagnetic
Radiation from Earthquakes

by

Mickey V. Ross
Lieutenant, United States Navy
B.S., United States Naval Academy, 1977

Submitted in partial fulfillment of the
requirements for the degree of

MASTER OF SCIENCE IN ELECTRICAL ENGINEERING

from the

NAVAL POSTGRADUATE SCHOOL
December 1984

Author:

Mickey V. Ross
Mickey V. Ross

Approved by:

R.W. Adler
R.W. Adler, Thesis Advisor

S. Jauregui Jr.
S. Jauregui Jr., Second Reader

Harriett E. Vigas
Harriett E. Vigas, Chairman,
Department of Electrical and Computer Engineering

John N. Dyer
John N. Dyer,
Dean of Science and Engineering

ABSTRACT

The design, construction, and testing of a freestanding radio frequency (RF) noise measurement and recording system in the 30 MHz and 150 MHz range is presented. Placement of the system along the San Andreas fault to permit the establishment of a correlation between increased background RF noise to earthquake fault activity for potential as an earthquake prediction tool is described.

TABLE OF CCNTENTS

I.	INTRODUCTION	11
A.	EVOLUTION OF EARTHQUAKE PREDICTION	11
B.	FOCUS OF STUDY	13
II.	BACKGROUND	14
A.	EARTHQUAKE GROUND MOTION	14
B.	SOURCES OF ELECTROMAGNETIC RADIATION IN EARTHQUAKES	15
1.	Insulators and Conductors	20
2.	Contact Electrification	22
3.	Fracture of Quartz-bearing Rocks	25
4.	Porous Rock	27
C.	SOURCES OF ELECTROMAGNETIC PRECURSOR EVENTS	32
1.	Electric Fields and Atmospheric Electric Potential	32
2.	Magnetic Fields and Animal Behavoir	33
III.	ELECTROMAGNETIC PROPOGATION CRITERIA FOR EARTHQUAKES	38
A.	THE ELECTRIC FIELD EQUATIONS	39
B.	SKIN DEPTH AND RADIATED FREQUENCIES	43
C.	THE PROPOGATION CRITERION	44
IV.	DESCRIPTION OF RESEARCH	46
A.	DESIGN GOALS	46
B.	SYSTEM COMPONENTS	49
1.	Receivers	49
2.	Recorders	52
3.	Interface Amplifiers	53

4. Timer	54
V. PERFORMANCE OF SYSTEM	62
VI. CCNCLUSIONS AND RECOMMENDATIONS	68
A. CONCLUSIONS	68
B. RECOMMENDATIONS	69
APPENDIX A: RECEIVER SENSITIVITY DATA AT VHF	
FREQUENCIES	70
APPENDIX B: ELECTROMAGNETIC EMISSIONS FROM	
EARTHQUAKES	73
A. COALINGA	73
B. RUSSIA	73
C. JAPAN	74
LIST OF REFERENCES	79
INITIAL DISTRIBUTION LIST	81

LIST OF TABLES

I.	Time Variations in the Geomagnetic Field	34
II.	Order of Magnitude Estimates of the Various Possible Physical Mechanisms for Earthquake-Related Field Anomalies	36
III.	Chart Speed and Trace Density	54
IV.	Frequency 38.45 MHz RF Input in uV and Signal Output in mV	71
V.	Frequency 150.75 MHz RF Input in uV and Signal Output in mV	72

LIST OF FIGURES

2.1	Elastic-Rebound Model of Earthquakes	16
2.2	Oblique View Across the San Andreas Fault Zone Typical Right-Lateral Offset of Stream Offset is About 450 Feet	17
2.3	Idealized Model of Earthquake Source	18
2.4	Double Couple Source Model of Fault Slippage Similar to Spheres Pulled by Wire Through Frictionless Tube	19
2.5	Shock-Induced Polarization Signals of Plexiglas Below Transition Pressure	21
2.6	Shock-Induced Polarization Signals of Plexiglas Above Transition Pressure	22
2.7	Shock-Induced Polarization Signals of Polystyrene Above and Below Transition Pressure . .	23
2.8	Shock-Induced Polarization Signals of Polystyrene and Plexiglas as a Function of Shock Pressure	24
2.9	Spectral Content of Fracture-Related EM Emission	26
2.10	Examples of EM Transients Accompanying Fracture of Piezoelectric Specimens	28
2.11	Electric Double Layer and Velocity Profile in a Capillary	29
2.12	Spectrum of the Geomagnetic Field	35
3.1	Cross-Section of Earthquake Fault Line	39
3.2	Electromagnet Vectors at Fault Hypocenter	41
4.1	Position of Antennas Along the San Andreas Fault	47

4.2	Block Diagram of Data Reception System	48
4.3	VHF Converter Schematic for 38.45 MHz	50
4.4	VHF Converter Schematic for 150.75 MHz	51
4.5	IF Audio Module Schematic	53
4.6	Rustrak Model 2146 Schematic	55
4.7	Rustrak Model 2146 with Signal Processor Schematic	56
4.8	Single Channel Modification (S-MOD)	57
4.9	Bias Stepper Demodification	58
4.10	Interface Amplifier with Voltage Generator	59
4.11	Time Tick Generator	61
5.1	Signal Level Data from Noise Measurement System . .	63
5.2	Signal Level Data from Noise Measurement System . .	64
5.3	Signal Level Data from Noise Measurement System . .	65
5.4	Signal Level Data from Noise Measurement System . .	66
5.5	Signal Level Data from Noise Measurement System . .	67
B.1	Earthquake Epicenter and HF Path Locations	74
B.2	Pseudo 3-D Plot of Doppler Disturbance Path	75
B.3	Electromagnetic Noise Levels at Caucasus	76
B.4	Electromagnetic Noise Levels at Sugadaira	77
B.5	Electromagnetic Noise Levels at Suginami	78

ACKNOWLEDGEMENTS

The author is indebted to a multitude of persons for their assistance and patience during the preparation of this thesis. Foremost, I wish to thank my Lord and Savior, Jesus Christ, whose grace I found sufficient.

I wish to express sincere gratitude to my wife, Mary, and my son, Timothy Joel, for confidence and assurance throughout this endeavor. I also wish to thank Dr. Richard W. Adler, and Dr. Stephen Jauregui, Jr., whose guidance and support were incessant. Finally, I wish to thank all the Naval Postgraduate School professors of whom I had classes under, CAPT Warren Averill, and the Bullard Hall gang for their superb support.

I. INTRODUCTION

A. EVOLUTION OF EARTHQUAKE PREDICTION

The problem involving searching for a reliable precursor to earthquakes is being given much attention throughout the world. With the reality that within minutes an earthquake can trigger an incredibly disastrous act of nature leaving death tolls in the tens of thousands and property damage in the billions anywhere in the world. The desire for prediction capabilities has evolved into an intense investigative scientific undertaking. Until recently, seismic activity data was collected only to establish where an earthquake has the greatest potential to occur. Hundreds of potentially destructive seismic shocks escape unnoticed because they occur in remote, sparsely populated areas of the earth.

The present state of the art in earthquake prediction may be compared to that of weather forecasting some 50 years ago. Seismological data acquired must be continuous and detailed from every area of the world that is subject to seismic disturbances. Various experimental methods for prediction of seismic activity are widely used such as electric and magnetic field, tilt, creep, and strain motion measurements to establish a practical data base [Ref. 1].

Evidence of radio (RF) emission associated with precursors to earthquake activity is very sparse. Electromagnetic radiation associated with earthquakes appears impulsively [Ref. 2], which suggests that these electromagnetic waves are radiated in a wide range of radio frequencies. The characteristics of the electromagnetic radiation depend greatly, however, on such factors as the magnitude of the earthquake,

and the large stress converts the insulating rock to a conductor or semiconductor. On reaching the brittle fracture stress, the material unloads and the stress is reduced and results in a retreating shock wave in the material. The shock wave has a conductor ahead of it with free electrons that can fall into the insulator conduction band behind the retreating shock front. The charges can accumulate by successive creep-slip motions to cause the electronic charge to produce an electrical field beyond the breakdown value in the air or rock surface, causing an arc with the attendant radio emissions.

3. Fracture of Quartz-bearing Rocks

The geological research group at the Los Alamos Scientific Laboratory were believed to be the first to detect radio frequencies when quartz-bearing rocks and other hard piezoelectric materials were fractured in laboratory experiments. Using a standard RF coil with a ferrite core placed about 5 to 50 CM from the sample and a transient recorder it was found that small cracks in quartz and tourmaline single crystals produce exponentially decaying RF transients with a time constant of about 10^{-5} seconds as shown in Figure 2.9 . Rock samples were fractured by applying uniaxial load between two parallel steel anvils or by pressing a small steel ball against a flat surface of the sample. The signal developed on the coil was amplified by a wideband amplifier and fed into one channel of the transient recorder. All measurements were performed under ambient conditions. Also the samples were not treated in any way except for cutting or coring [Ref. 9].

The fact that the fracture related EM emission was observed only in quartz and tourmaline crystals and in quartz-bearing rocks rules out triboelectric effects (frictional electricity) as the source of this emission and indicates that it is related to piezoelectricity. The most

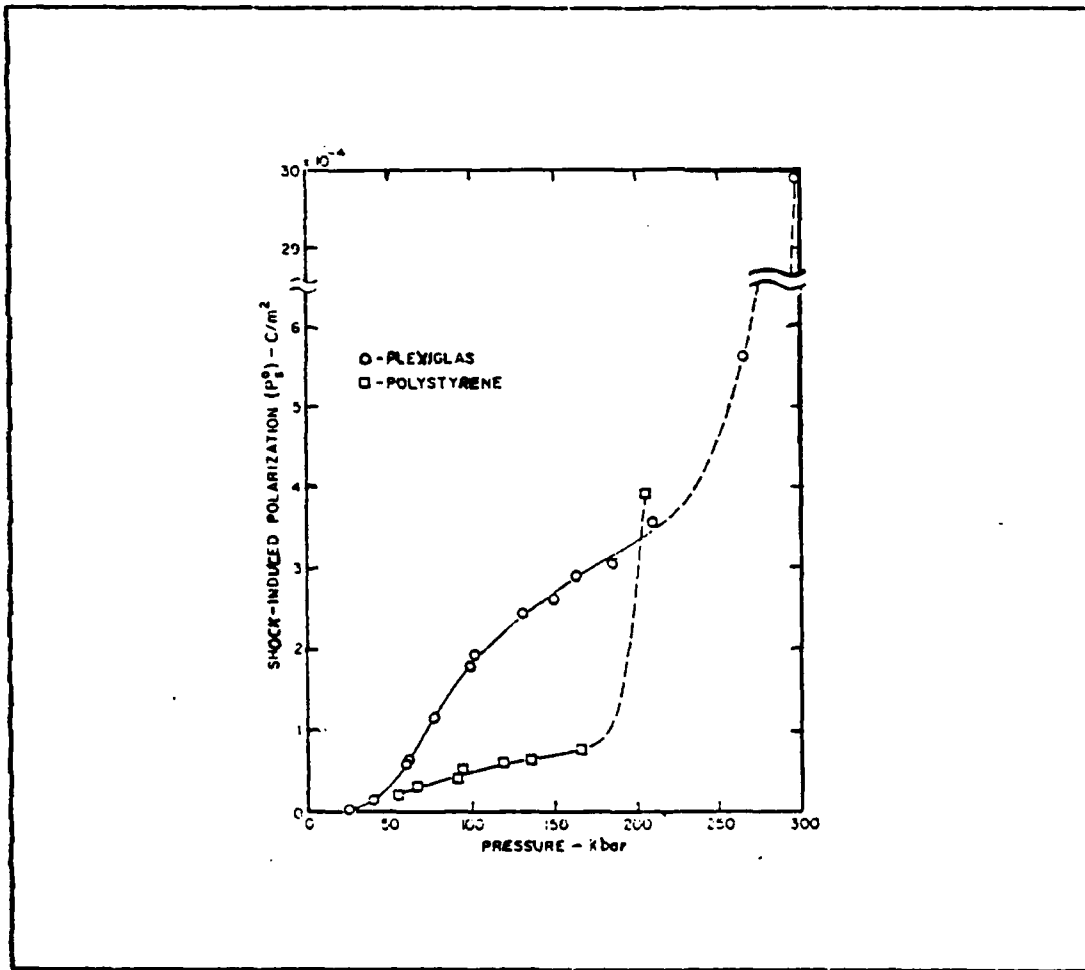


Figure 2.8 Shock-Induced Polarization Signals of Polystyrene and Plexiglas as a Function of Shock Pressure

sliding must exist if the boundary layer consists of dielectric or semiconducting matter and this electrostatic component is an appreciable part of the force of sliding friction [Ref. 8].

Active fault lines move by relaxation oscillations and can be described by the nonlinear stick-slip motion that is generated when the static force of friction is larger than the kinetic frictional value. During the increasing stress, the motion of the fault proceeds uniformly by creep

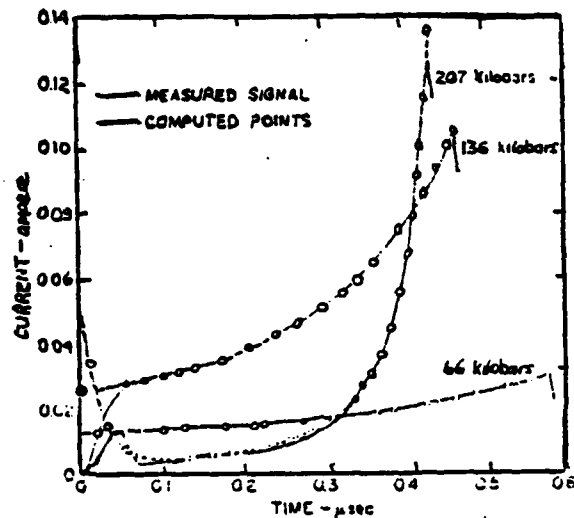


Figure 2.7 Shock-Induced Polarization Signals of Polystyrene Above and Below Transition Pressure

exhibiting two characteristics, that of relaxation oscillation. The first is a fixed amplitude and the second is a period determined by a relaxation time for the building up of a limiting value. The experiments described the amplitude of the jerks was observed to decrease when the dielectric breakdown strength of the material used as a lubricant was diminished, or when, with the same lubricant, the velocity of sliding was increased. Observations of contact electrification show that an electrostatic force resisting

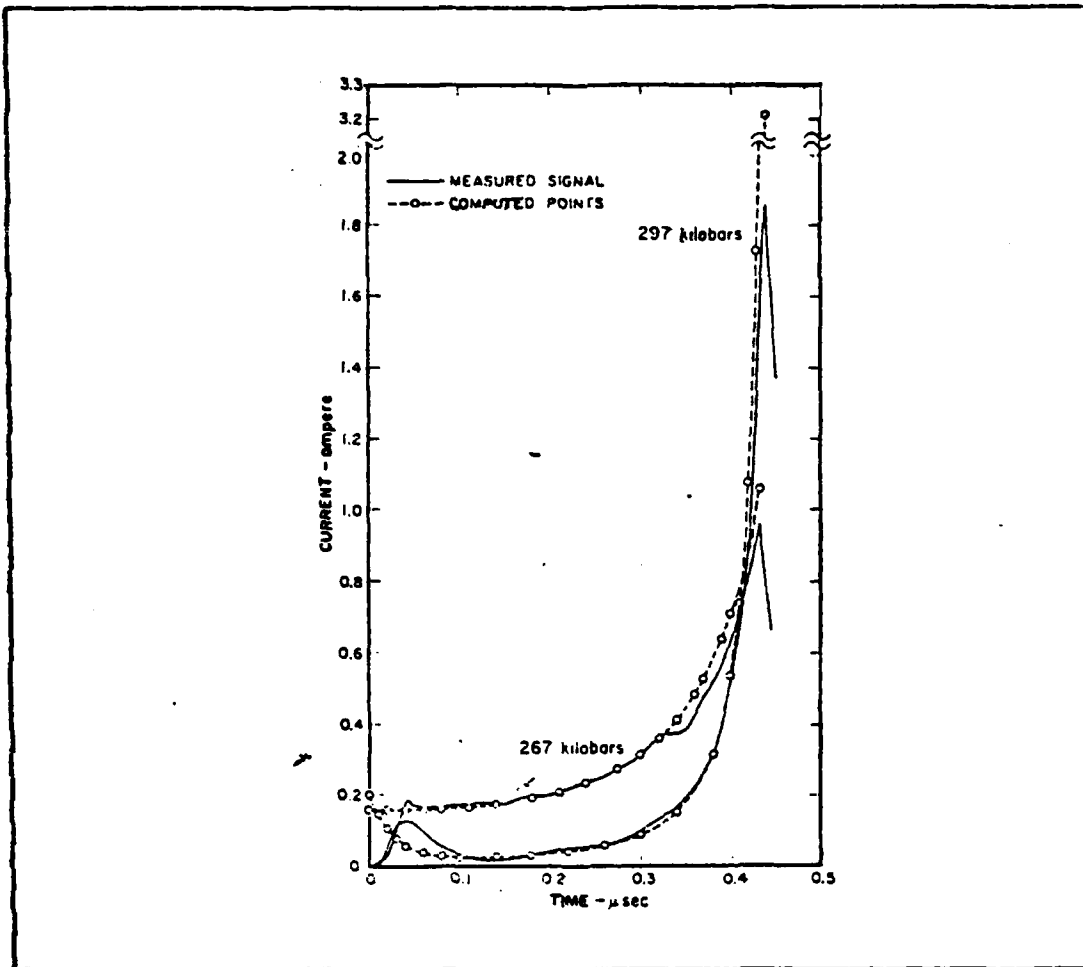


Figure 2.6 Shock-Induced Polarization Signals of Plexiglas Above Transition Pressure

signals at low pressures than at high pressures where the ends of the measured signals are more distorted by curvature and obliquity of the shock front.

2. Contact Electrification

Electrification of insulators and conductors by impact are described in experiments conducted by Schnurmann and Warlow-Davies of two metals separated by an insulating oil. Slow sliding can proceed by a series of jerks

motion would result in a larger polarization of the material by both mechanical and electrical forces in agreement with the observed increase in both P_s and K' at the phase

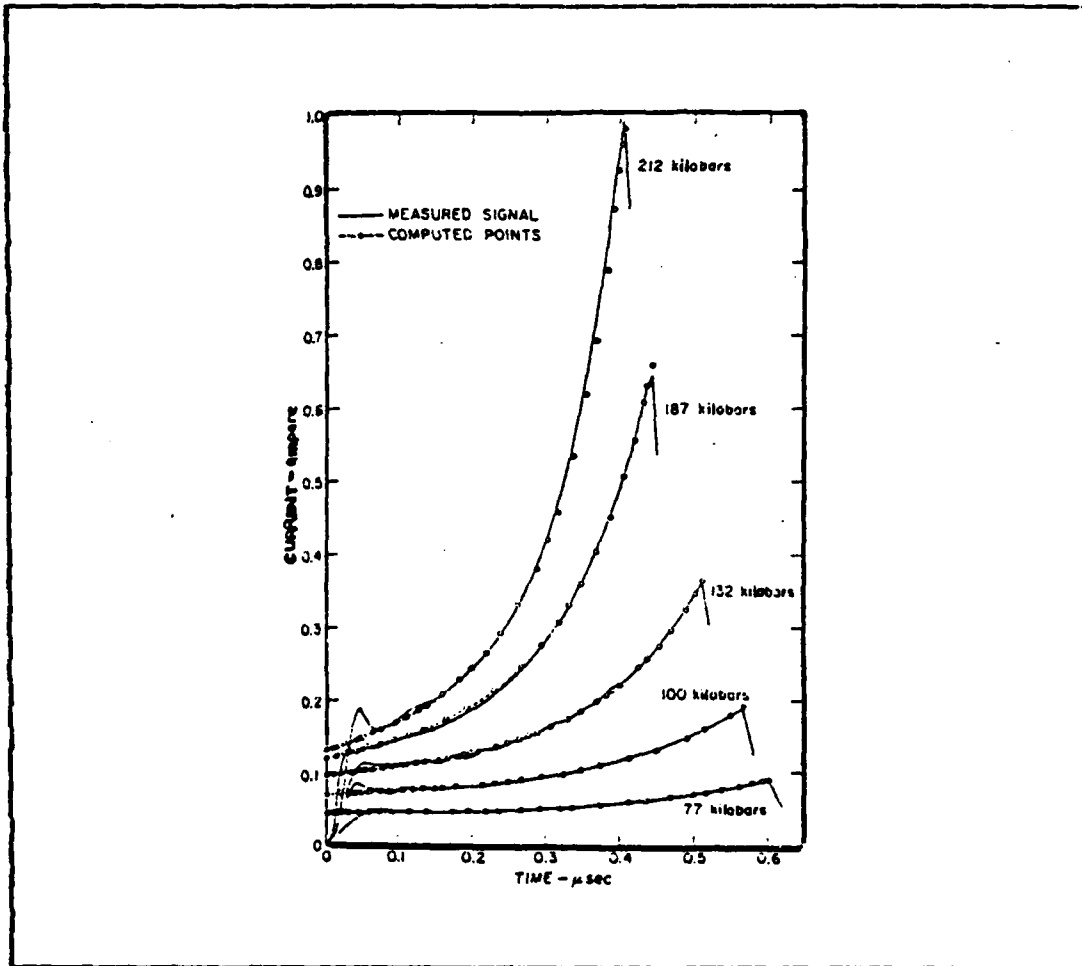


Figure 2.5 Shock-Induced Polarization Signals of Plexiglas Below Transition Pressure

transition. Figures 2.5, 2.6, 2.7, and 2.8 show that over the entire pressure range of the measurements, the polarization signals can be described by a physical model involving three variables, P_s , K' , and γ . It should be noted that the computed curves are in better agreement with measured

sliding during stress increases and stick-slip motion during the stress release.

1. Insulators and Conductors

The radio emission theory rests on the principle that an insulator can be mechanically stressed to become a conductor or semiconductor with subsequent charge migration from the conducting rocky material to the insulating rock under the equivalent electric field generated by a shock wave during brittle fracture of the rock. Experimental evidence from the Ballistic Research Laboratory, Aberdeen Proving Ground, Maryland showed that shock-induced polarization is an increasing function of pressure [Ref. 7].

At low pressures shock-induced polarization (P_s) becomes small but is easily measured down to approximately 25 Kbar. Shock-induced polarization of both plexiglas and polystyrene was observed at lower pressures, but the noise level associated with the experiments prevented accurate measurement. At high pressures data indicated transitions P_s began a more rapid increase, suggesting transitions to a state where the plexiglas and polystyrene were more easily polarized by the shock wave.

The dielectric constant of the shocked medium, K' , was also an increasing function of pressure. The values for K' were characterized by appreciable scatter, but indicated a gradual increase up to the transition pressure where a more rapid increase was noted. The relaxation time, τ , was also characterized by appreciable scatter, but remained between 0.5 and 1.5 μsec up to the transition pressure, where a rapid decrease began. If it is assumed that polarization is caused by the motion of atoms or atomic groups, then the sudden decrease in τ suggest that motion occurs more freely in the high pressure phase, and that the transitions are to a more fluid state. Greater freedom of

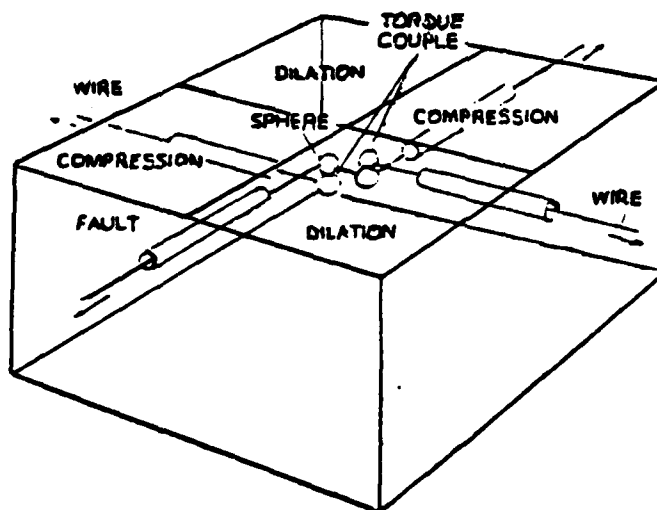
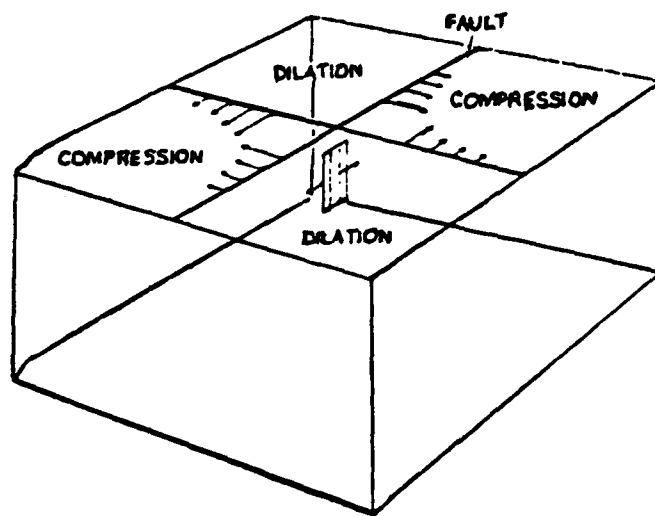


Figure 2.4 Double Couple Source Model of Fault Slippage
Similar to Spheres Pulled by Wire Through Frictionless Tube

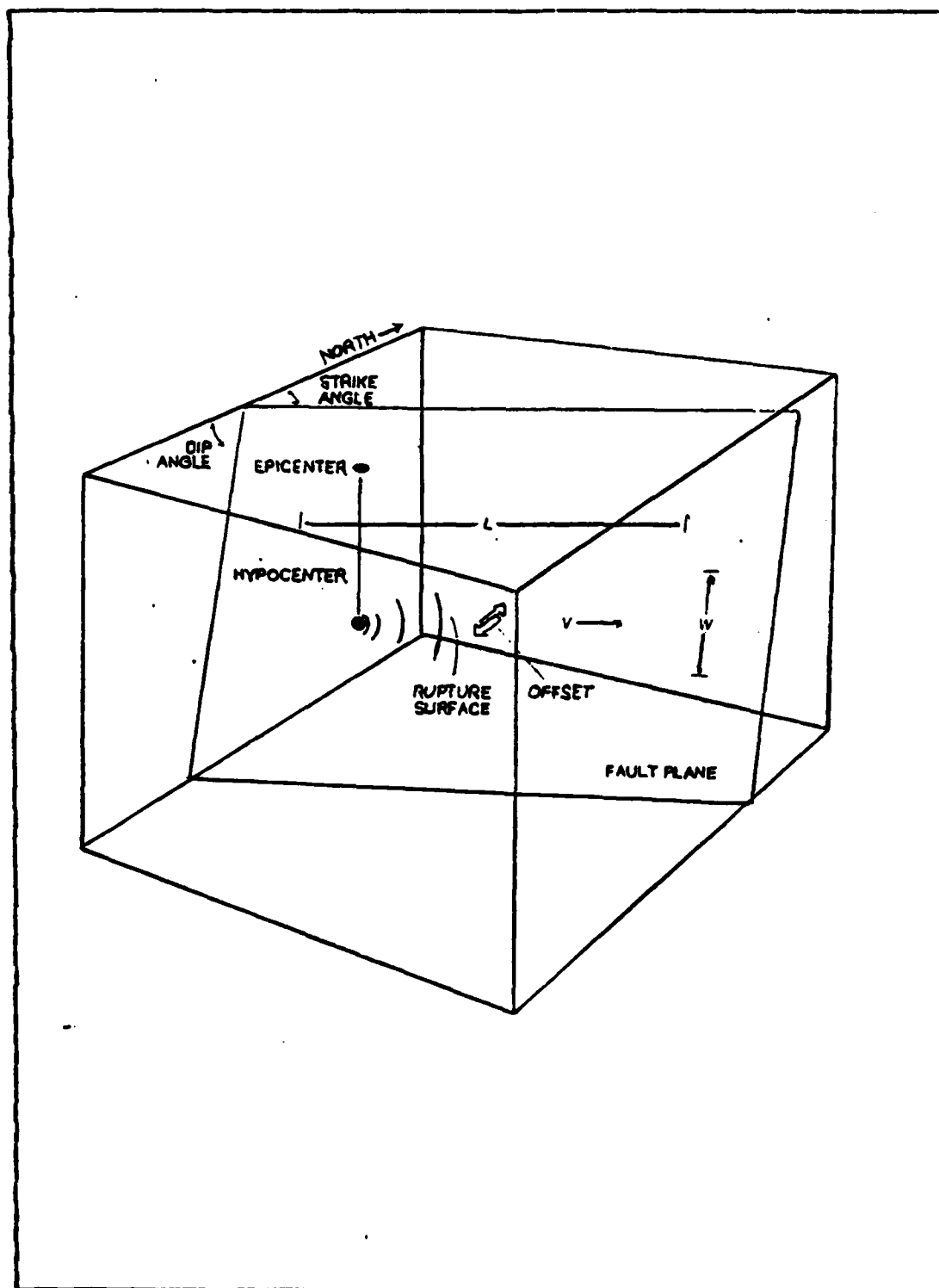


Figure 2.3 Idealized Model of Earthquake Source



Figure 2.2 Oblique View Across the San Andreas Fault Zone
Typical Right-Lateral Offset of Stream
Offset is About 450 Feet

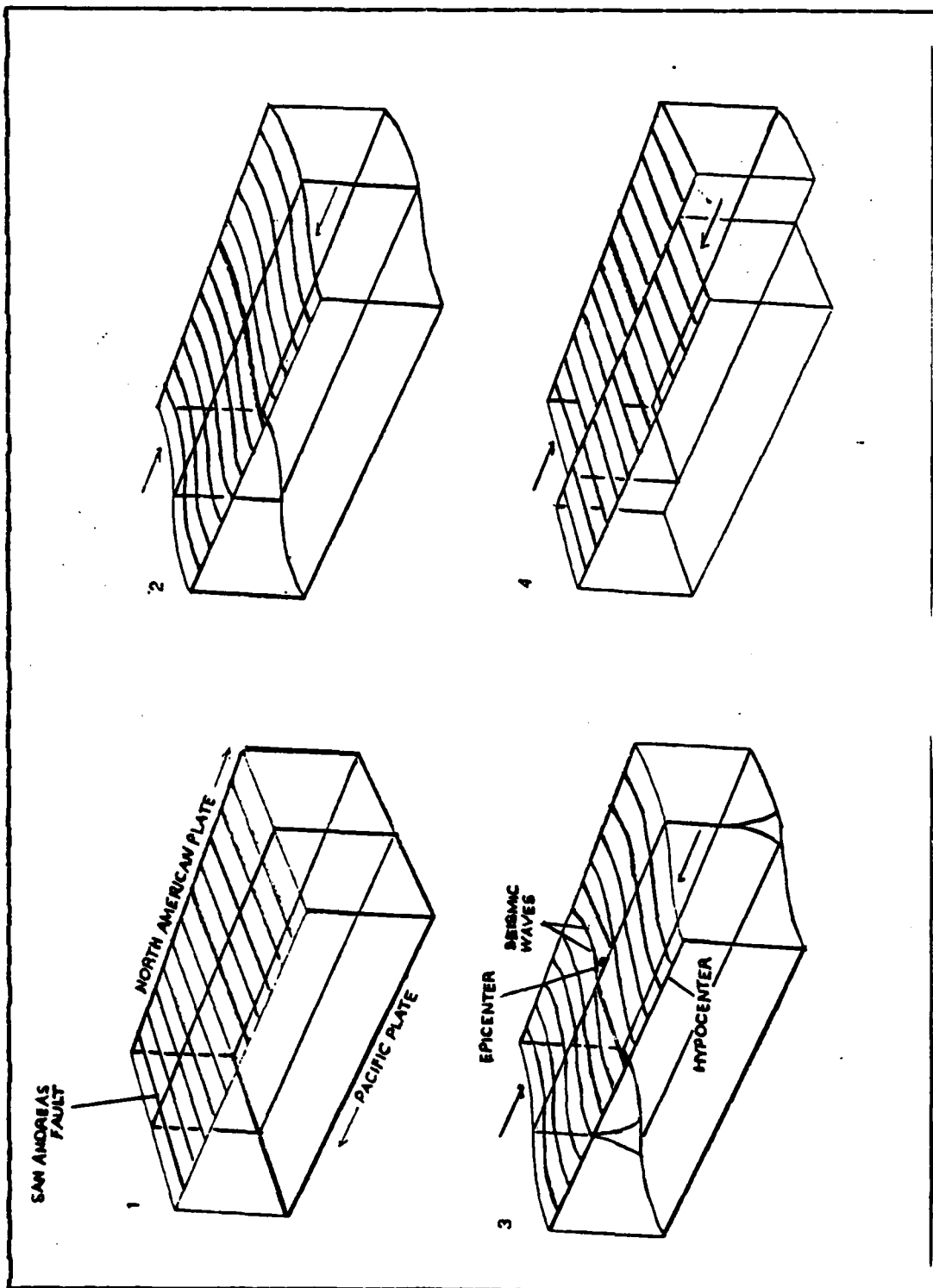


Figure 2.1 Elastic-Rebound Model of Earthquakes

energy radiated over ground at any one time may be quite small. This slow process is referred to as a seismic slip or creep.

Most earthquakes are generated in zones where the huge plates of the lithosphere, which make up the outer layer of the earth's surface, as in Figure 2.1 and Figure 2.2 [Ref. 6], are shearing past each other. A conceptual model of the faulting process, as in Figure 2.3 and Figure 2.4, were largely developed from investigations of earthquakes along the San Andreas fault. Over the past 137 years, more than 20 severe earthquakes have been recorded in the state of California, mainly along the San Andreas fault. The San Andreas fault which extends from the Gulf of California in the South to Cape Mendocino varies in width from about a meter to 1.6 KM, and plunges almost vertically into the earth for 15 to 20 KM. These are some of the reasons why the San Andreas qualifies for conducting an intensive, longterm RF noise measurement investigation to show anomalous increases in the intensity of electromagnetic radiation precursor to earthquakes.

B. SOURCES OF ELECTROMAGNETIC RADIATION IN EARTHQUAKES

The emissions of RF are theorized to be caused by the increasing of mechanical pressure at the fault causing shear stresses that convert the insulating rock to a conductor (or semiconductor) by reducing the energy gap between the valence and conduction bands. During the stress increase, microfractures cause shock waves that accelerate the electrons in the conducting bands to radiate both acoustic and electromagnetic energy. If the mechanical forces increase to the yield point, the rock fails in brittle fracture and causes a sudden decrease in the shear forces. The mechanical motion is described by a stick-slip motion that has stable

II. BACKGROUND

A. EARTHQUAKE GROUND MOTION

Equally important to predicting the occurrence of an earthquake is determining which of the many ways the ground is likely to shake during the earthquake, how strong the shaking will be, and how long it will last. Knowledge of ground motion can make it possible to understand the characteristics of the earthquake source. Most measurements made during actual earthquakes at seismological stations are some distance from the source. The localized source of an earthquake was not observed for its significance until the San Francisco earthquake of 1906.

It was recognized that slippage along a fault in the earth's crust caused the earthquake. The classic study of Harry F. Reid of Johns Hopkins University revealed that rocks parallel to the fault had been strained or sheared. From the basis of his geodetic observations emanated the elastic rebound theory of earthquakes which asserts that rocks are elastic, and mechanical energy can be stored in them just as it is stored in a compressed spring [Ref. 5].

When two blocks forming the opposite sides of a fault move by a small amount, the motion elastically strains the rocks near the fault. The frictional bond fails at its weakest point when the stress becomes large enough. That point of initial rupture, called the hypocenter, may be near the surface or deep below it. The seismic waves radiate from the hypocenter in all directions producing the earthquakes. The point on the surface of the earth above the hypocenter is the epicenter of the earthquake. The rocks rebound over an interval of minutes, days or even years. The seismic

density to produce the electric field and subsequently the specific surface area behaves as a constant current generator.

B. FOCUS OF STUDY

The design, construction, and testing of a freestanding radio frequency (RF) noise measurement and recording system in the 30 MHz and 150 MHz range is presented. Placement of the system along the San Andreas fault to permit the establishment of a correlation between increased background RF noise to earthquake fault activity for potential as an earthquake prediction tool is described.

the depth of focus, the geology of the earthquake region, the distance between epicenter and point of observation, the condition of ionospheric propagation, and others. This is possibly the reason why the intensity of the electromagnetic radiation is different for different earthquakes, with values varying from tens or hundreds of microvolts per meter up to tens of hundreds of volts per meter.

Measurements are presently being made to explore the possibility of the existence of electro-magnetic fields. However, there presently appears to be no directed research, or a plausible explanation for, reported radio frequency emission interference coinciding with an increase in earthquake activity. Derr noted an observation of noise on the FM broadcast band (88-108 MHz) occurring simultaneously with earthquake lights [Ref. 3]. The reception of earth-based 18 MHz radio noise by J.W. Warwick of the High Altitude Observatory, Boulder, Co. at the time of the famous Chilean earthquake still has been unanswered [Ref. 4]. Research personnel involved in RF interference study, in interviewing citizen band and amateur radio operators in the Hollister, Ca. area, noted a consistent report of "increase in background noise level preceding earthquake activity" in the frequency range of CB (27 MHz) and six and two meter amateur bands (50-54 MHz and 144-148 MHz). Reports typically cited a noticeable (10 dB) increase in background noise which preceded an earthquake by 12 to 24 hours, returning to normal just before the tremors were felt (one hour to 15 minutes). Observations of the electrostatic field (field mills) have reported that diurnal variations at selected sites are accompanied by "high frequency, spiky noise" that apparently have no explanation. Various theories have been approached on what is actually occurring at the fissure boundary, whether impact of dissimilar materials or shock induced polarization have developed the necessary charge

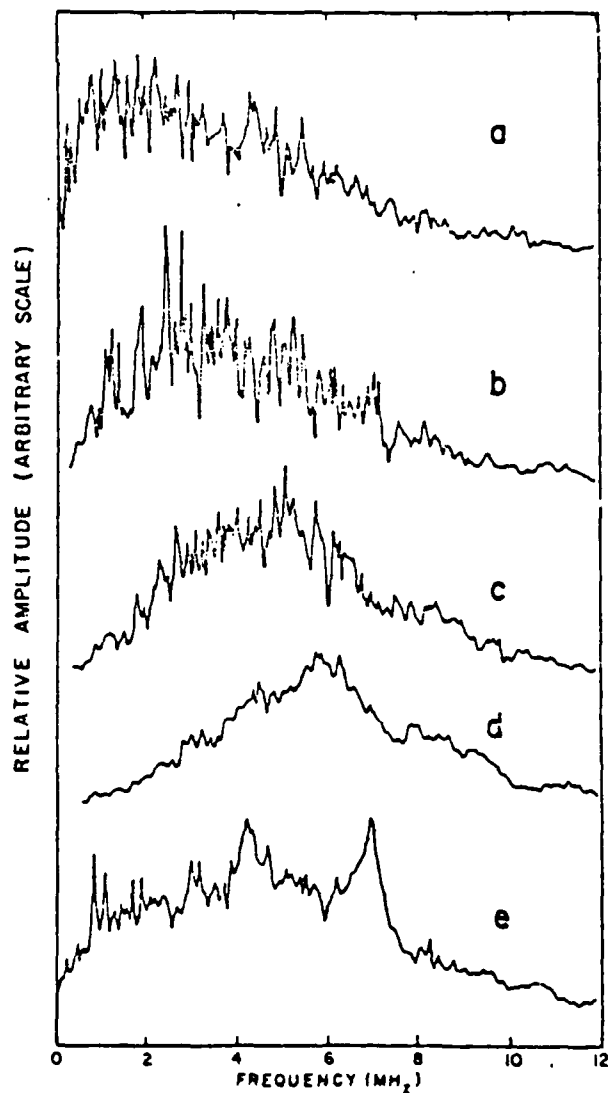


Fig. 2. Spectral content of fracture-related EM emission from (mean grain size shown in brackets): a. coarse-grain granite (15 mm); b. granodiorite (2 mm); c. fine-grain granite (from Westerly, R. I., 0.5 mm); d. fine-grain quartzite (0.1 mm); e. a 2 x 1 x 0.5 cm tourmaline single crystal cracked by applying pressure along the c axis. The curves show averages of 10 spectra for each sample.

Figure 2.9 Spectral Content of Fracture-Related EM Emission

probable mechanism for this emission is the rapid drop in the piezoelectric field accompanying the sudden release of stress when fracture occurs as shown in Figure 2.9 . This hypothesis is supported by the observation that the amplitude of the resulting RF signal is independent of load, since regardless of the stress distribution within the sample fracture occurs only when the local stress exceeds a specific value (much higher than the average stress in the experiments) and therefore drop in stress is essentially independent of load.

Figure 2.10 compares the spectral content of fracture related EM emission from several samples, obtained by averaging 10 different spectra for each sample. It is clear that a shift to higher frequency occurs as the grain size of quartz-bearing rocks decrease.

Detection and analysis of fracture-related RF signals was very difficult at distances greater than 50 cm. With regard to RF emissions outside of the laboratory, no conclusions could be made from the study concerning whether a substantial increase in the size of the fracture results also in a corresponding increase in the emitted RF energy, thereby permitting detection at larger distances.

4. Porous Rock

Electrokinetic phenomena induced by ground water flow associated with earthquakes are believed to provide a possible means of earthquake prediction. Detectable variations of earth currents, electric potential and geomagnetic field may be caused by diffusion of fluid into a dilatant (wider or larger) focal region. The electrokinetic phenomena controlled by the processes of mineralized water migration through microcapillary rock channels are an independent source of charge separation and relaxation. The charge

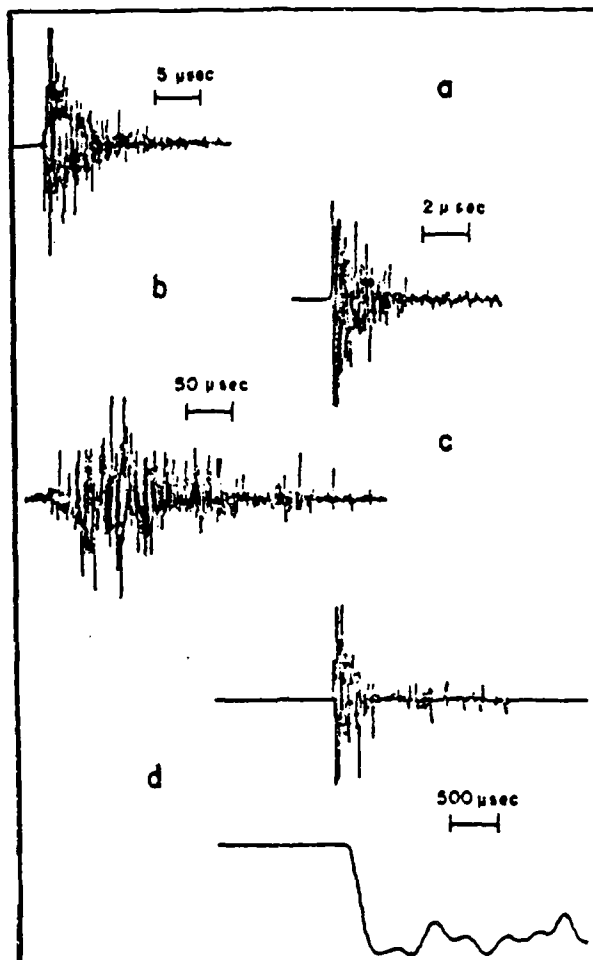


Fig. 1. Examples of EM transients accompanying fracture of piezoelectric specimens (the digital sampling interval is given in brackets): a. small crack in a quartz single crystal (50 ns); b. small crack in a tourmaline single crystal (10 ns); c. failure of a specimen of fine grain sandstone (200 ns); d. failure of a quartzite specimen, showing also the accompanying drop in load (2000 ns, see text). Note the different time scale for each transient.

Figure 2.10 Examples of EM Transients Accompanying Fracture of Piezoelectric Specimens

separation is due to the selective absorption of ions from the solutions on the fracture surfaces and the formation of double electric layers.

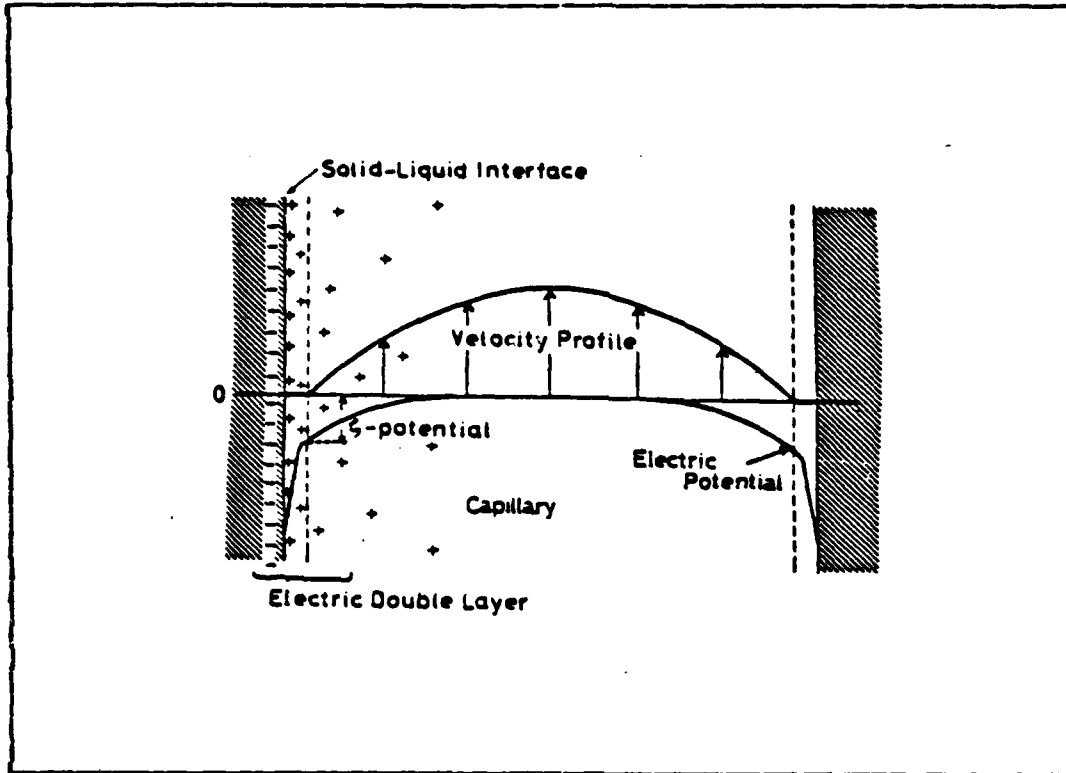


Figure 2.11 Electric Double Layer and Velocity Profile in a Capillary

The double layer is made up of a layer of ions which are firmly held to the solid, and a more diffuse mobile layer extending into the liquid phase. The resultant charge of the diffuse layer is equal in magnitude but of opposite sign to that of the firmly held layer. A simplified schematic diagram of the structure of the double layer and profiles of the electric potential and velocity of liquid in a capillary is shown in Figure 2.11. Because of the electrical charges, there is a difference of electrical potential between the

solid-liquid interface and the bulk of the liquid. This is called the electrokinetic potential or zeta potential. When an electromotive force (EMF) is applied to an electric double layer, there will be a displacement of the oppositely charged layers relative to one another. If the solid cannot move, the fixed part of the double layer also is unable to move; the application of an EMF will result in movement of the diffuse layered ions and liquid [Ref. 10].

Applied EMF and viscous force is given by:

$$j = (\epsilon \zeta / \eta) \text{ grad } E \quad (2.1)$$

where j is the fluid flow flux (volume) through a capillary per unit time and per unit area, ζ is the zeta potential, η is the viscosity of the fluid, and ϵ is the dielectric constant of the fluid.

The streaming potential (E) is the production of a potential difference when a liquid is forced through a porous medium or a capillary tube. It is given by

$$\text{grad } E = - (\epsilon \zeta / \eta \sigma) \text{ grad } P \quad (2.2)$$

where σ and P are the electrical conductivity and the pressure of the fluid, respectively.

Since all electrokinetic processes are irreversible, the thermodynamics of an irreversible process can be applied. The most general relations between the electric current i and the fluid flow j , and the forces of $\text{grad } E$ and $\text{grad } P$ are

$$-i = L_{11} \text{ grad } E + L_{12} \text{ grad } P \quad (2.3)$$

$$-j = L_{21} \text{ grad } E + L_{22} \text{ grad } P \quad (2.4)$$

where L_{ij} are constants. Explicit expressions of L_{ij} 's for a capillary tube are:

$$L_{11} = \sigma \quad (2.5)$$

$$L_{12} = L_{21} = -\epsilon \zeta / \eta \quad (2.6)$$

$$L_{22} = k^* / \eta \quad (2.7)$$

where k^* is the specific permeability of the capillary tube.
For porous media k is given by

$$k = \phi k^* \quad (2.8)$$

where ϕ is the porosity of the porous media. The basic equations of fluid flow in the porous medium are

$$-I = \phi \sigma \text{ grad } E - (\phi \epsilon \zeta / \eta) \text{ grad } P \quad (2.9)$$

$$-J = -(\phi \epsilon \zeta / \eta) \text{ grad } E + (k / \eta) \text{ grad } P \quad (2.10)$$

It is assumed that the electrical conductivity of a matrix substance is much smaller than $\phi \sigma$.

The maximum magnitude of the current density associated with the water flow is obtained by setting $\text{grad } E = 0$:

$$-I = (\phi \epsilon \zeta / \eta) \text{ grad } P \quad (2.11)$$

This shows the electric current is proportional to the pore pressure gradient (the pore pressure is assumed to change by 10 - 1000 bars in the dilatant focal region preceding or following the earthquake). If the mean gradient of pore pressure is approximated to be

$$\overline{\text{grad } P} = 1 \approx 100 \text{ bar/Km} \quad (2.12)$$

the electric current induced is

$$|I| = 0.7 \times (10^7 \approx 10^8) \text{ A/m}^2 \quad (2.13)$$

If the capability of detecting the water flow exists, the direction of water flow can be known, and consequently predict the epicenter of the earthquake. The earth current due to electrokinetic effects yields variations of the geomagnetic field on the surface.

If the current flows uniformly in a horizontal circular cylinder of radius R , the magnetic field caused by the current is simply obtained by Biot and Savart's law,

$$H = (I / 2\pi r) \cdot \pi r R^2 \quad (2.14)$$

where r is the distance from the center of the cylinder to the point at which the magnetic field is observed. If

$$r = R = L / 2 \quad (2.15)$$

then the field strength becomes

$$H = 0.2 \approx 200 \gamma \quad (2.16)$$

where the field strength is independent of R and L for this assumed geometry. Interestingly enough most observed magnitudes of magnetic anomalies associated with earthquakes are almost all in the range estimated above.

C. SOURCES OF ELECTROMAGNETIC PRECURSOR EVENTS

1. Electric Fields and Atmospheric Electric Potential

At the earthquake moment and just before it the effects due to disturbances of natural electromagnetic earth

field (NEMEF) were observed repeatedly. These effects involve quasi-stationary disturbances of the atmospheric electric potential (AEP) up to 1000 V/m, at distances up to some hundred kilometers from the epicenter. In the course of field observations the AEP perturbations were noted some hours before the earthquake moment within one or two hours period [Ref. 11].

AEP disturbances estimated for the charged surface are:

$$E_{AEP} = \sigma / 2 \epsilon_r \epsilon_0 \quad (2.17)$$

where

$$\sigma = q N \delta \quad (2.18)$$

Under the assumptions that the linear charge density q , the surface density N , and the dislocation path length are:

$$q = 10^{-14} - 10^{-10} \text{ C/m} \quad (2.19)$$

$$N = 10^9 - 10^{11} \text{ m}^2 \quad (2.20)$$

AEP disturbances of 100 - 1000 V/m can be expected in the final stage of the earthquake precursor period.

2. Magnetic Fields and Animal Behaviour

The amplitude and time duration of the most characteristic time varying geomagnetic disturbances occurring at the earth's surface are listed in Table I. Another way of presenting the same data is in a plot of the spectrum of the total magnetic field. Such a spectrum is shown in Figure 2.12 [Ref. 12], where skin depth ($Z = 500 (\sigma f)^{-0.5}$) is plotted as a function of frequency f and conductivity σ . It

TABLE I
Time Variations in the Geomagnetic Field

Characteristic Period (secs)	Description of Phenomena	Typical Magnitude (gamma)
10^{-2}	Sub-audio frequency fluctuations	0.01 sec^{-1}
10^0	Micro-pulsations	0.1
10^2	Giant pulsations	10
	Sudden commencements	20
	Crochets	20
	Bay Phenomena	100
10^4	Diurnal variation	30
10^6	Storm Time effects	10
	Twenty-seven day recurrence effects	8
10^8	Annual variation	10
	Solar cycle secular variations	25 year^{-1}

is evident that the most dominant signals are the diurnal, semi-diurnal, twenty-seven day (due to the rotation of the sun) and high frequency changes that are, in general, non-stationary, that is not frequency stable. This spectrum could represent also a crude measure of discrimination limits for detection by animals. It is, of course, possible that animals can somehow understand these variations well enough to detect changes well below the background variations. Schemes for doing this are necessary also for field experiments presently in operation on the San Andreas Fault where information on the large scale of these disturbances is used to enhance detection capability for local magnetic field

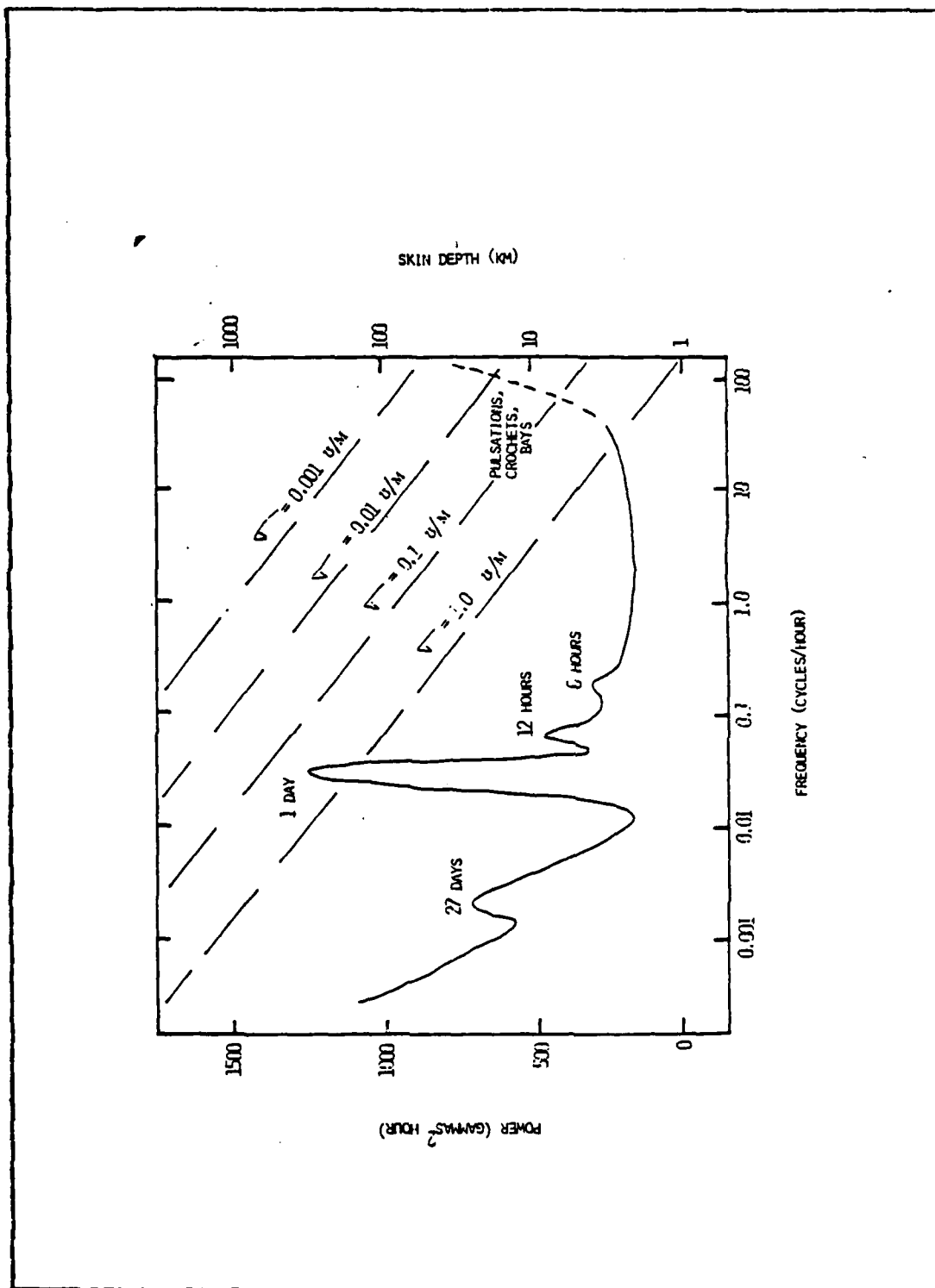


Figure 2.12 Spectrum of the Geomagnetic Field

variations [Ref. 13]. If animals can detect effects occurring days before an earthquake, it is possible that these effects involve systematic change which would enhance the spectrum over a critical frequency range.

There are a number of physical mechanisms that might be considered as sources for earthquake-related animal

TABLE II

Order of Magnitude Estimates of the Various Possible Physical Mechanisms for Earthquake-Related Field Anomalies

A. MAGNETO HYDRODYNAMIC

$$\Delta B_{\text{INDUCED}} = B_0 \sigma \mu v d \approx 0.1 \text{ gamma}$$

(σ = conductivity, $\mu = 4 \times 10^{-7}$, v = velocity, d = length scale)

B. TELLURIC CURRENTS

$$\Delta B_{\text{INDUCED}} = \sigma E / D \approx 0.01 \text{ gamma}$$

(σ = conductivity, E = geoelectric field, D = depth of current flow)

C. PIEZO MAGNETIC EFFECT

$$\Delta B = 40 S I \approx 1 \text{ gamma}$$

(S = stress change, I = magnetization)

D. LOCALIZED CRACKS AND FRACTURES

$$\Delta B = ?$$

behavior. Table II lists several of these together with order of magnitude estimates of their amplitudes. It would appear that for these effects at least, it is difficult to generate source amplitudes of more than a few tens of gammas. The last process suggested which involves this

concerns the relatively unknown electrical and magnetic effects of local surface cracks and fractures might be a possible exception to this.

III. ELECTROMAGNETIC PROPOGATION CRITERIA FOR EARTHQUAKES

A geological fault line becomes a source of acoustic, thermal and electromagnetic radiations when the tectonic plates move relative to each other. The region near the fault line, shown in Figure 3.1 is in both shear and compressive stress and the relative permittivity, ϵ_r , is greater here than in the unstressed region having permittivity ϵ_r . The fault width of $2Y_0$ is the region of uniform stress and the regions beyond this point are unstressed.

When fault line motion commences, a voltage is generated causing current flow across an interface between two different materials. The interface can be formed by the following means:

a. Forces near 100 Kbars can convert the insulating rock to a semiconductor (or conductor) in solid form [Ref. 14] so that charges can flow at the insulating-semiconductor interface which is also the voltage generating mechanism since the work functions differ in the two media.

b. Forces above 100 Kbars may cause plastic rock flow to produce a liquid-solid interface [Ref. 15] with differing work functions causing current flow and charge storage in the solid portion having insulating properties.

c. Shock waves can distort the dipole fields in the rock to produce a polarization in the material and increase the permittivity by nearly an order of magnitude [Ref. 16]. The transient charge is stored on the lower permittivity regions and accumulates with subsequent shocks.

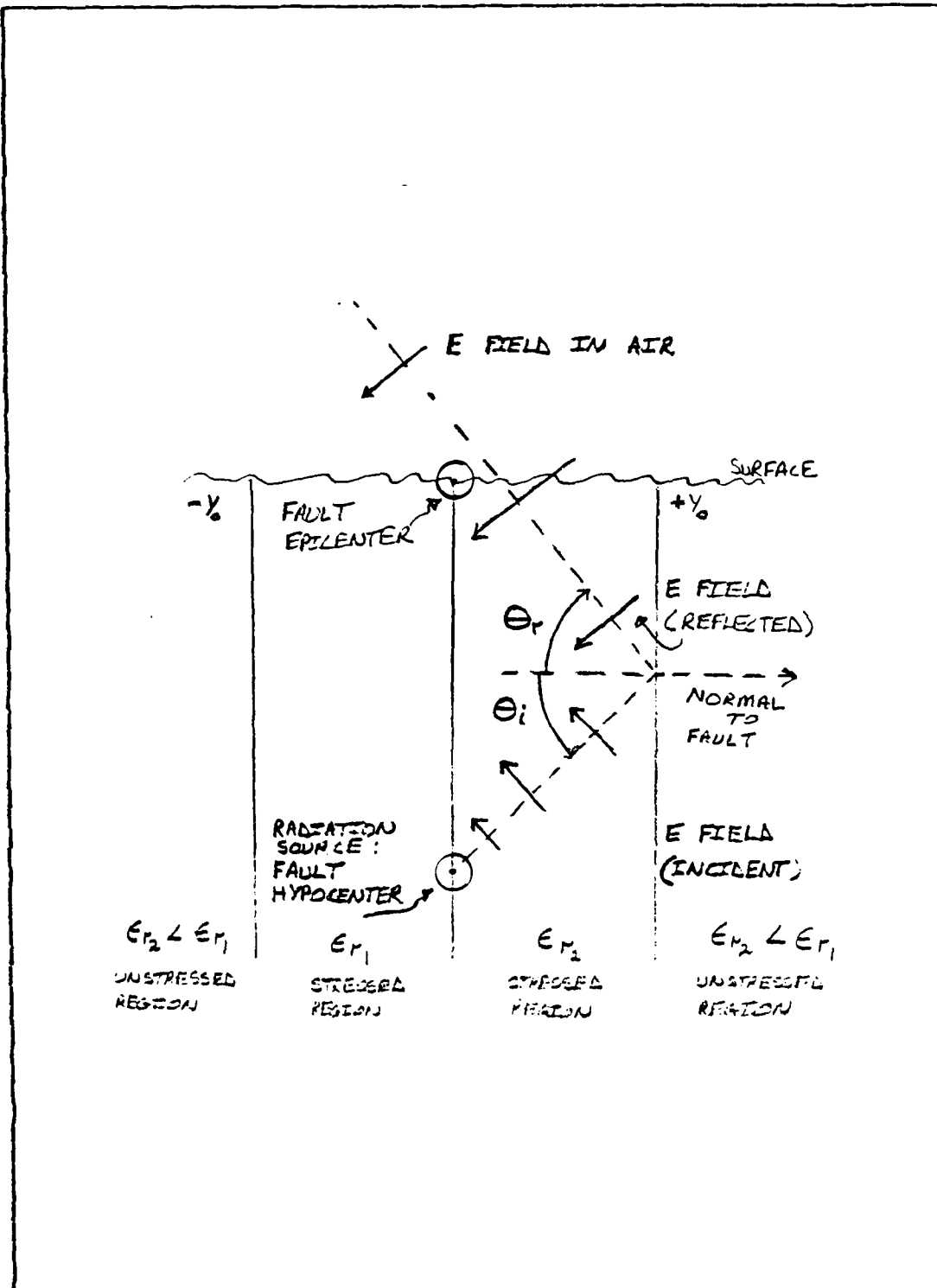


Figure 3.1 Cross-Section of Earthquake Fault Line

The 10.7 MHz signal is converted to 455 KHz and amplified by three stages. Each stage consists of several transistors biased from an integral zener regulated source. An optimally coupled three stage IF filter provides selectivity against adjacent channel interference. Figure 4.5 shows a schematic diagram of the IF Audio Module. Appendix A contains Table IV and Table V, data of receiver signal output voltages for a given RF signal input voltage at both VHF assigned frequencies. The output capabilities of the receiver were determined from this information on the S-meter (output signal to the chart recorder).

2. Recorders

The Rustrak DC recorder prints through the impinging action of its stylus driven by the chopper bar against pressure-sensitive chart paper. Its presentation is a series of dots appearing as a continuous line. Writing speed varies with motor speed. Chart speed and trace density depend on the ratio of the interchangeable gear box which couples the paper drive to the motor. Table III shows the chart speed and trace density. Figure 4.6 is a schematic of the Model 2146 dual trace chart recorder and Figure 4.7 is a schematic of the same model with a signal processor included as shown. Both versions of Model 2146 had to be modified for single channel use. The single channel modification (S-MOD) involved bypassing a switch (S-2) by putting a small jumper wire between the normally closed (N/C) and the normally open (N/O) terminals as shown in Figure 4.8. Three of the recorders have signal processors to desensitize the signal input to one volt per division. The desensitizer board was demodified by rearranging the bias stepper connections at the Jones plug making non-bias stepper connections as shown in Figure 4.9. There were no modifications necessary for the Model 388 chart recorder.

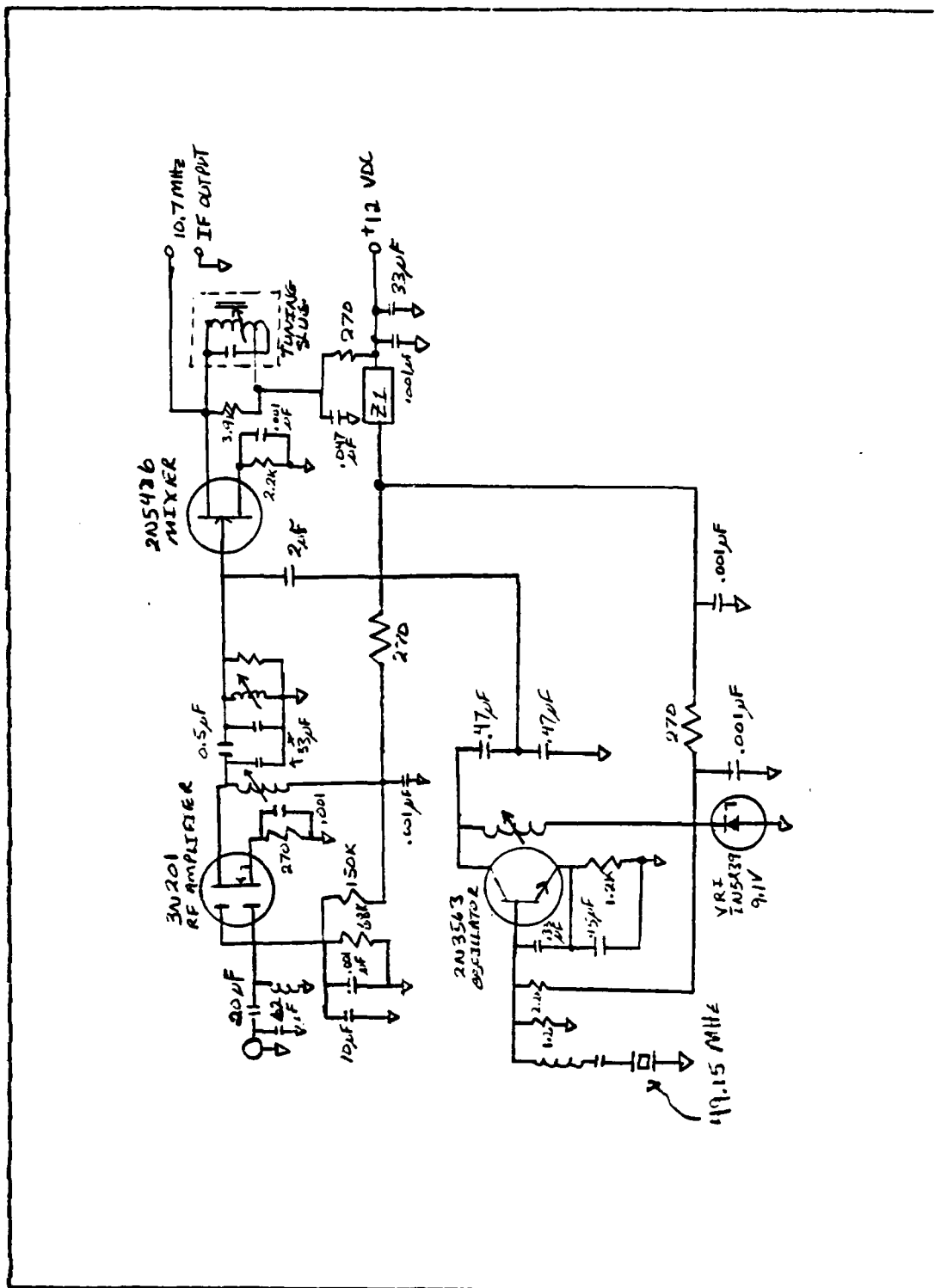


Figure 4.3 VHF Converter Schematic for 38.45 MHz

Low cost modularized receivers were procured and modified to receive at the assigned frequencies. The output of the receiver is offset to nullify any ambient noise level and is fed into slow speed chart recorder to collect any detected emissions as a function of time. A block diagram of the measurement system is illustrated in Figure 4.2 . The noise measurement system can operate from 12 volt DC storage batteries or a power supply. The chart paper and storage batteries have to be replaced periodically. Electromagnetic emission data collected through this system will be related to seismic quake data provided by the United States Geological Survey Office, Palo Alto, Ca.

B. SYSTEM COMPONENTS

1. Receivers

The VHF Converter Module is designed to amplify and convert the specific frequency to the HF range. The converter is supplied with a 10.7 MHz intermediate frequency (IF) transformer for the mixer output circuit. The mixer output circuit consists of a slug tuned coil, a capacitive voltage divider, and an RCA jack to provide a 50 ohm output. Figures 4.3,4.4 show schematic diagrams of the VHF Converter Modules.

The IF Audio Module comprises a highly sensitive and selective IF amplifier, AM detector, audio amplifier, and squelch system for use with the converter to make a VHF communications receiver. The selectivity of the unit was tailored to operate in the noise measurement system. The unit has automatic gain control (AGC) of both IF and RF, with the RF AGC being delayed for best response. An integral log detector provides drive for the "S" meter (signal to Rustrak recorder) output.

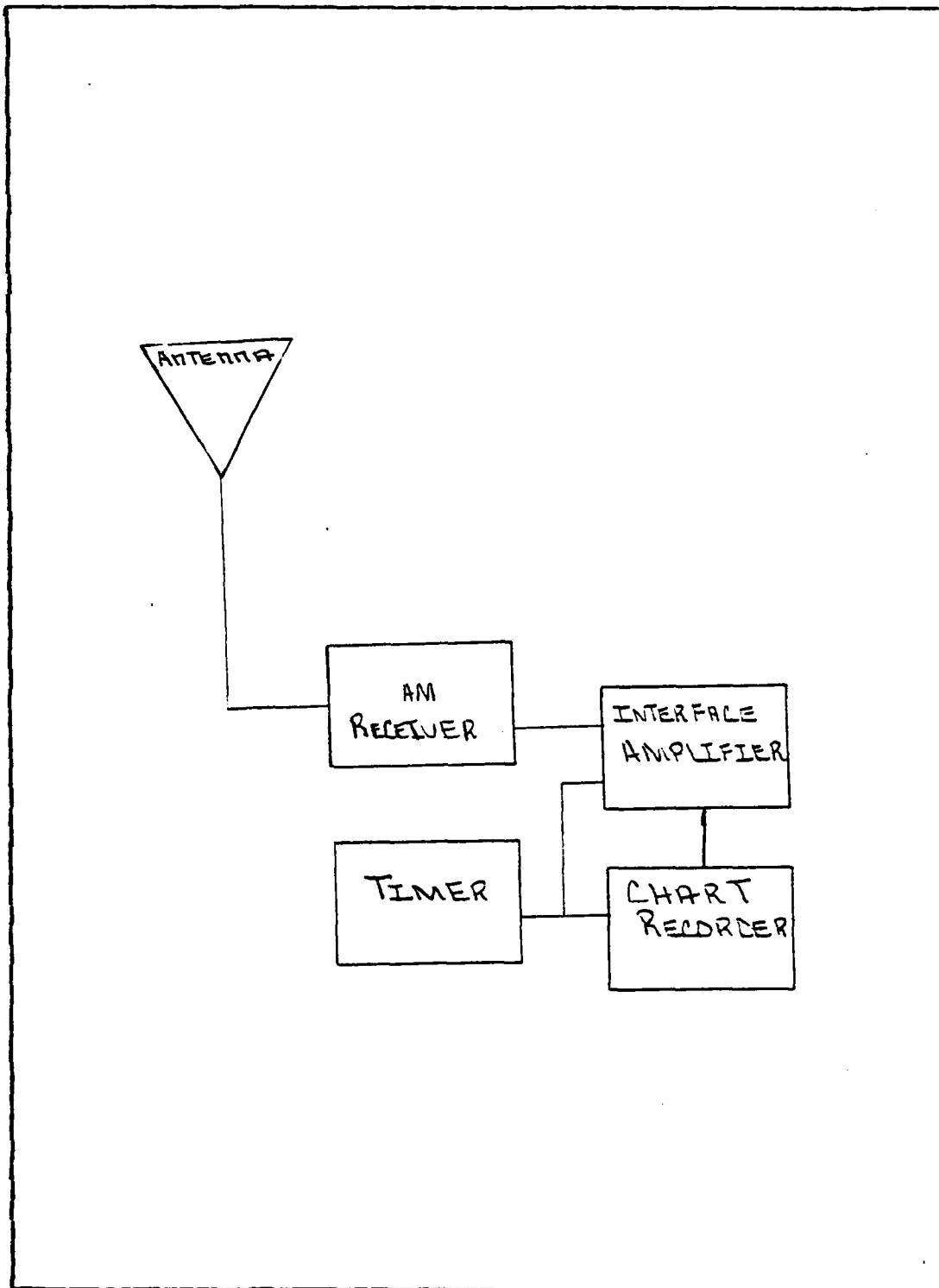


Figure 4.2 Block Diagram of Data Reception System

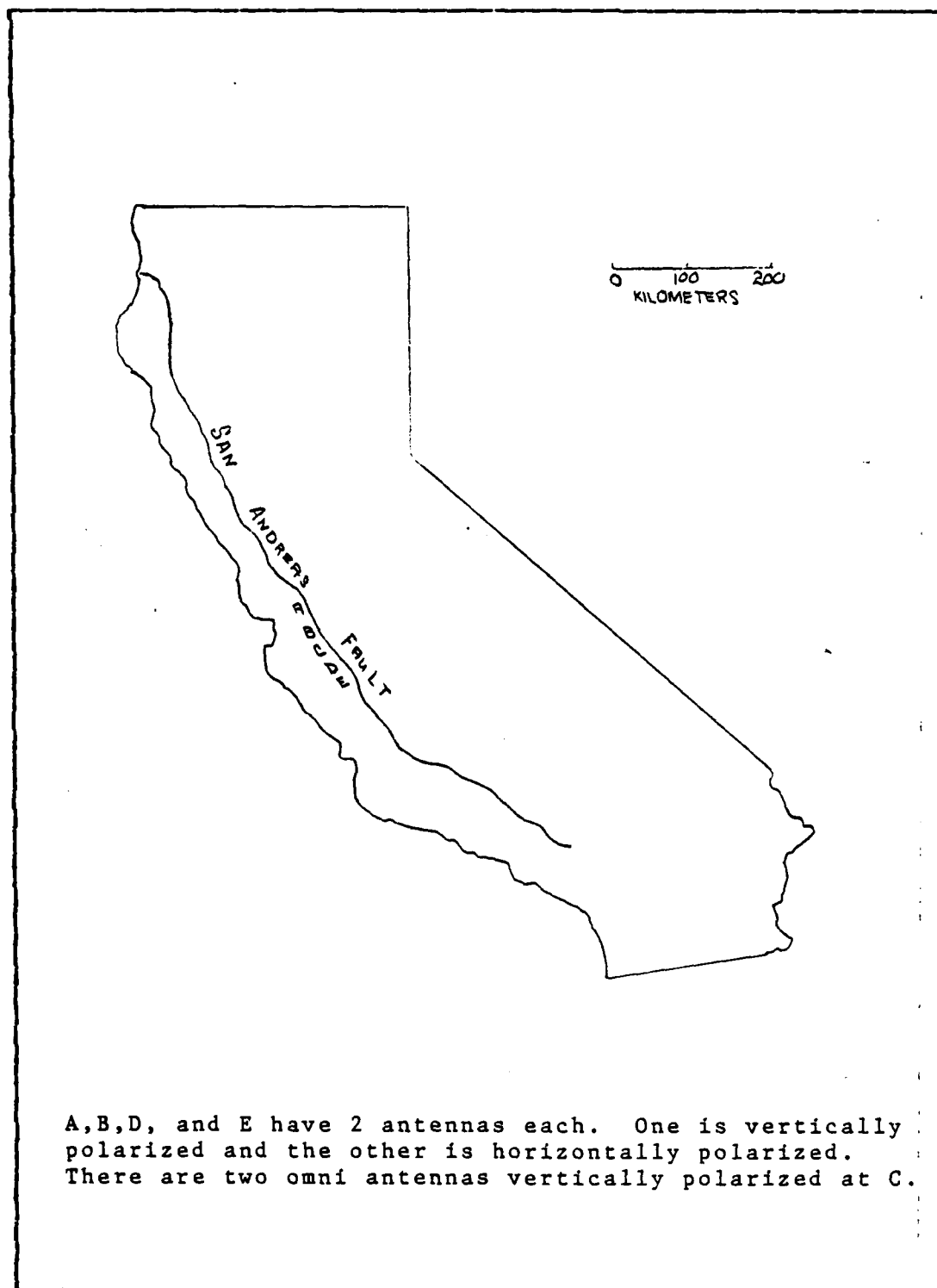


Figure 4.1 Position of Antennas Along the San Andreas Fault

IV. DESCRIPTION OF RESEARCH

A. DESIGN GOALS

One of the most important problems associated with using electromagnetic radiation as a precursor of earth quakes is how to select the point of observation. Placement of the system far from industrial areas, but near potential earthquake activity was desired. A preliminary field survey of potential site locations was conducted under the direction of the United States Department of the Interior, Geological Survey. Site location along the San Andreas fault was chosen because of it being known historically and recently as an active earthquake area. The chosen observation site is 1000 feet from the San Andreas Rift Zone (fault) located at $121^{\circ} 23.5' W$ and $36^{\circ} 45.5' N$ which is three miles east of San. Juan Bautista and seven miles south of Hollister.

It became very important to secure spot window frequencies for the system so not to have any interference from transmitted radio waves. The Army Frequency Coordinator for the Western United States identified and assigned to this project VHF bands (38.45 MHz and 150.75 Mhz). These frequencies, with a 50 KHz bandwidth, have been allocated with exclusive use for a period of one year.

For observation of signal intensity and direction in the VHF range, a data recording system was positioned with its directional sensors (antennas) looking both up and down the fault as shown in Figure 4.1. The antennas (eight Yagi's) detect both horizontally and vertically polarized emissions at both reserved frequencies. The omnidirectional antennas (two) are erected for detection at both frequencies, and with vertical polarization. Each of the ten antennas are connected to a detector (communications receiver).

$$\theta_i = \sin^{-1}(0.2)^{.5} = \sin^{-1}(0.45) \approx 26^\circ \quad (3.24)$$

Since the critical angle is small, the majority of the radio emissions are reflected from the unstressed region for hypocenters deep in the fault. This wide region of radio emission may account for the abnormal human and animal behavior distant from the fault line but within the stressed fault region. When the field in the air space above the epicenter exceeds 30 Kv/cm, the air breaks down and confirms the reports of lightning before and during large earthquakes.

under the worst case of the hypocenter at the extreme depth, the electrical field is reduced slightly more than $1/e$, but easily measured at the epicenter.

The values of permittivity and conductivity vary with frequency and the upper limit of propagating frequency can be estimated from the graph by Kraus and Carver [Ref. 17]. Using the worst case of urban ground at 100 megahertz, the skin depth is about 0.8 Km and if the hypocenter is halfway down the 15 Km tectonic plates, the attenuation is $e^{-2.5}$. This limits the radiation to the range $5 \times 10^7 < f < 10^8$ Hz.

C. THE PROPOGATION CRITERION

Figure 3.1 shows the radiation source at the hypocenter and the electric field, parallel to the incident plane, makes an incident angle θ_i with the normal to the fault. The reflected wave is at an angle θ_r with the normal. The stressed region has a width $2Y_0$ and $\epsilon_{r_1} > \epsilon_{r_2}$. If the regions are insulating and lossless, the reflection coefficient is given by:

$$\rho = E_r / E_i \quad (3.21)$$

$$= \frac{\cos \theta_i - \sqrt{\frac{\epsilon_2}{\epsilon_1} - \sin^2 \theta_i}}{\cos \theta_i + \sqrt{\frac{\epsilon_2}{\epsilon_1} - \sin^2 \theta_i}} \quad (3.22)$$

The reflected wave, E_r , equals the incident wave, E_i , when the radical in the numerator vanishes. The critical value of the incident angle for complete reflection is:

$$\sin \theta_{ic} = (\epsilon_2/\epsilon_1)^{.5} = (\epsilon_{r_2}/\epsilon_{r_1})^{.5} \quad (3.23)$$

This relation obtains for either perpendicular or parallel polarization of the electric field and for all $\epsilon \geq \theta_{ic}$. Using $\epsilon_{r_1} = 25.0$ for the stressed region and $\epsilon_{r_1} = 5.0$ for the unstressed portion, gives

B. SKIN DEPTH AND RADIATED FREQUENCIES

In Figure 3.1, the fault line region which has a constant compressive and shear stress is region one, and the unstressed region, away from fault line, designated region two. The permittivities and conductivities in the two regions are:

$$\epsilon_1 = \epsilon_{r1} \epsilon_0 \quad (3.13)$$

$$\sigma_1 = \sigma_1 \quad (3.14)$$

$$\epsilon_2 = \epsilon_{r2} \epsilon_0 \quad (3.15)$$

$$\sigma_2 = \sigma_2 \quad (3.16)$$

Where ϵ_0 is the permittivity of free space and ϵ_{r1} and ϵ_{r2} are the relative permittivities. The skin depth, δ , is the distance where the radiation is reduced by the factor of $1/e$ from the initial value. The skin depth can be obtained from equations:

$$\delta = 2\omega\epsilon_1 / \sigma_1 = 2\omega\epsilon_1 \epsilon_0 / \sigma_1 \quad (3.17)$$

Using:

$$f = 5 \times 10^7 \text{ Hz}, \omega = 100\pi \times 10^6 \text{ Hz}, \sigma_1 = 10^{-5}, \quad (3.18)$$

$$\epsilon_{r1} = 25.0, \quad \epsilon_0 = 8.8 \times 10^{-12} \quad (3.19)$$

$$\delta = 13.9 \text{ Km} \quad (3.20)$$

Since the San Andreas fault is about 15 Km deep, the skin depth is less than this value which indicates that

The parallel E vector mode, where the E field is in the incident plane, can be obtained from the vector equations to obtain the scalar differential equations:

$$-\partial H_z / \partial x = \sigma E_y + \epsilon \partial E_y / \partial t \quad (3.3)$$

$$\partial E_y / \partial t = -\mu \partial H_z / \partial x \quad (3.4)$$

Let the arc discharge have the spectrum $f_1 < f < f_2$ and $\omega = 2\pi f$. If $E = E_0 \cdot e^{j\omega t}$, the scalar field reduces to:

$$\partial E_y / \partial x - \gamma^2 E_y(x, t) = 0 \quad (3.5)$$

where

$$\gamma^2 = j\omega\mu\sigma - \omega^2\mu\epsilon \quad (3.6)$$

Assume a scalar solution with $E = E_0 \cdot e^{-\gamma x} \cdot e^{j\omega t}$. This gives the phase shift and attenuation:

$$\gamma = (\mu\omega)^{.5} (j\sigma/\omega\epsilon - 1) \quad (3.7)$$

$$= j(\mu\omega)^{.5} (1 - j\sigma/\omega\epsilon)^{.5} \quad (3.8)$$

$$= j(\mu\omega)^{.5} (1 - j\sigma/2\omega\epsilon + \dots) \quad (3.9)$$

$$\approx j(\mu\omega)^{.5} (1 - j\sigma/2\omega\epsilon) \quad (3.10)$$

$$\approx j(\mu\omega)^{.5} + \sigma/2\omega\epsilon \quad (3.11)$$

The radiating field has the form:

$$E = E_0 e^{-x \frac{\sigma}{2\omega\epsilon}} e^{x j \sqrt{\mu\omega}} e^{j\omega t} \quad (3.12)$$

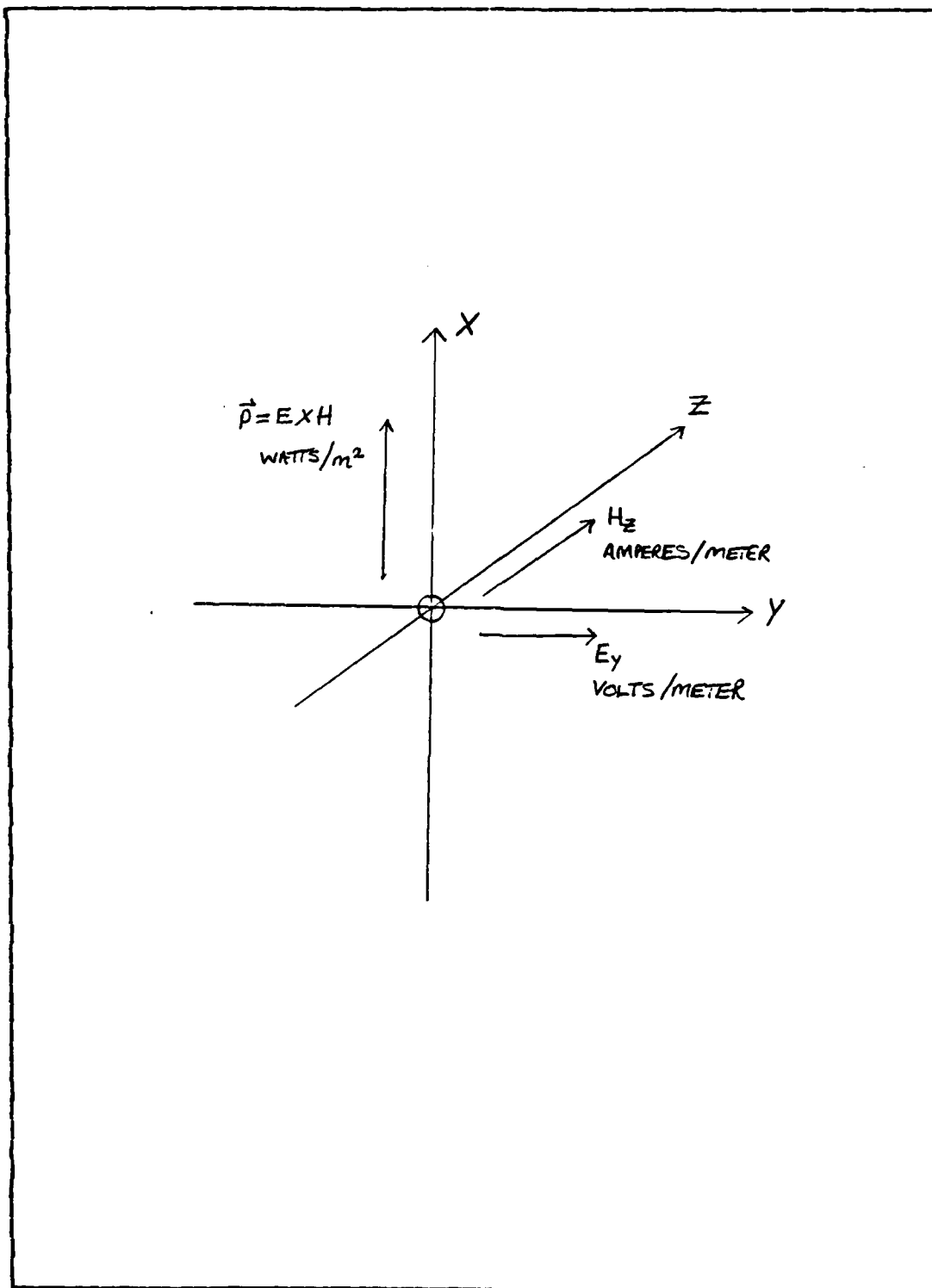


Figure 3.2 Electromagnet Vectors at Fault Hypocenter

A. THE ELECTRIC FIELD EQUATIONS

The source of the electromagnetic radiations is the discharge of the accumulated electrons that were formed by shock waves or increasing pressures on the fault. A continuous corona discharge can occur from the nonuniform fields that form on sharp points of the rock or a sudden discharge can result when the field exceeds the breakdown strength of the rocks in uniform or nonuniform fields. If the breakdown occurs in microseconds, radio waves in the megahertz region are radiated. This increasing pressure at a fault can be related to the strength and frequency spectrum of radiations which can be correlated to the acoustic data presently being recorded at the earthquake sites.

The fault hypocenter, shown in Figure 3.1 is usually below the surface and is the source of the electromagnetic radiation, shown as a point source. The emissions are probably elliptically polarized but only the parallel field is depicted for clarity. Figure 3.2 shows the electric field vector, E in volts/meter in the incident X-Y plane and the magnetic field vector, H in amperes/meter, normal to the incident plane. The energy propagates on the transverse mode (TEM) and the Poynting vector, P in watts/square meter, on the X axis.

The fault epicenter is shown in Figure 3.1 and is the location of the hypocenter at the fault surface where the electromagnetic radiations are a maximum.

The electromagnetic radiations can be obtained from the retarded potential method but the objective is to only indicate the attenuation of the field with distance which can be found from the Maxwellian equations:

$$\nabla \times \vec{H} = \vec{D} + \epsilon \partial E / \partial t \quad (3.1)$$

$$\nabla \times \vec{E} = -\mu \partial H / \partial t \quad (3.2)$$

TABLE III
Chart Speed and Trace Density

Model	Drive Motor Speed (RPM)	Writing Speed	$\frac{2}{30:1}$	$\frac{6}{10:1}$	Gear Train No. Gear Ratio
2194	1	1 strike/4 seconds		3 in/hr 76 mm/hr 252 hrs	Chart Speed Chart Speed Paper Duration
388	2	1 strike/2 seconds	2 in/hr 50 mm/hr 378 hrs		Chart Speed Chart Speed Paper Duration
Trace Density			900	300	Strikes/Inch

3. Interface Amplifiers

By design the receiver output voltages were approximately between 280 mV to 320 mV with RF inputs from approximately 10 uV to 100 uV. Ideally this 40 mV range would drive the recorder from zero to full scale, but because of an op amp voltage offset only 80 % scale readings were achieved. An interface amplifier was designed to set full scale minimum and maximum needle movement in the chart recorder. Calibration of the meter movement was accomplished by variable resistor settings as shown in the schematic of Figure 4.10 .

4. Timer

To compare seismological disturbance data with the noise measurement site recordings accurate time needed to be

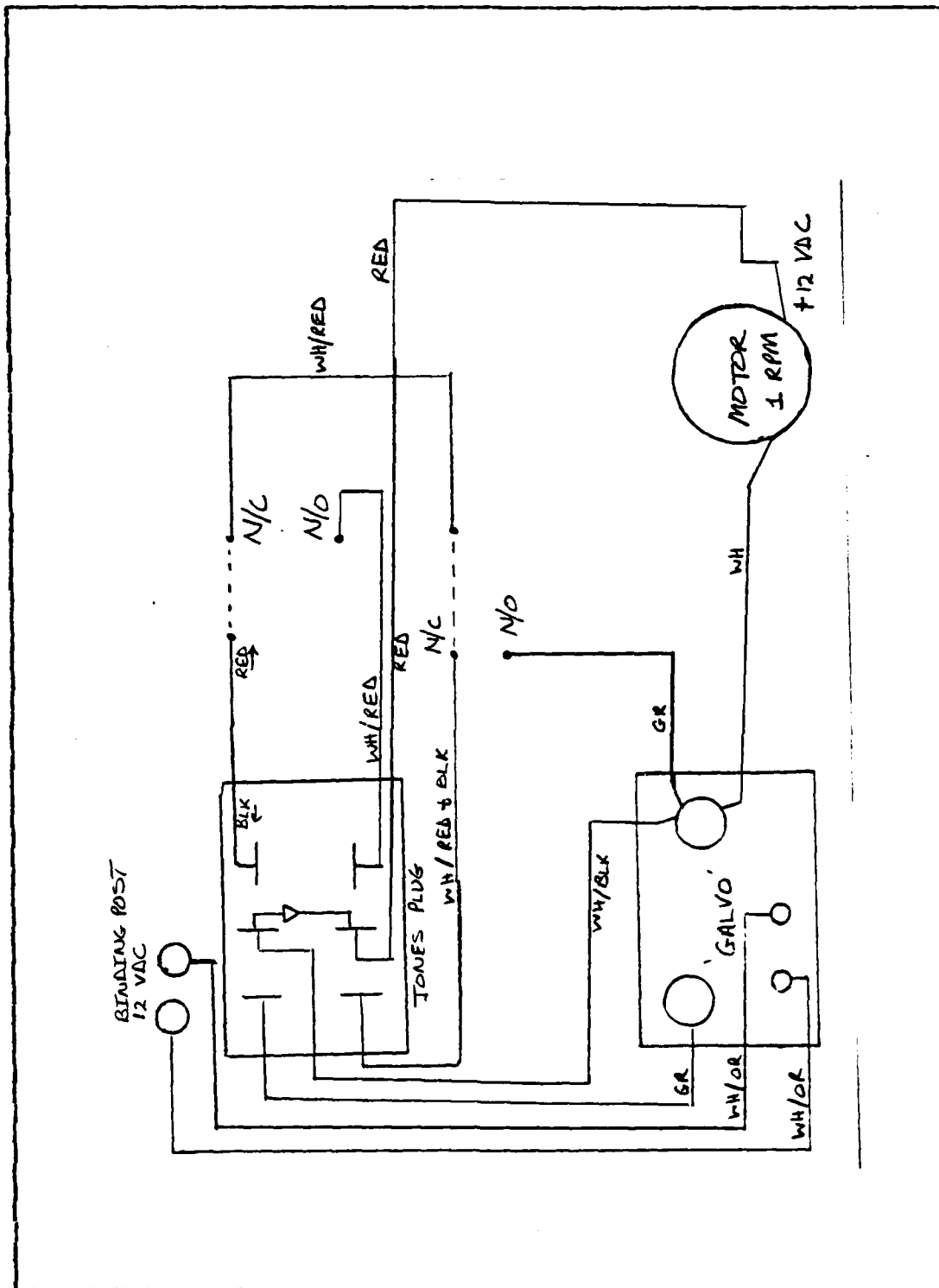


Figure 4.6 Rustrak Model 2146 Schematic

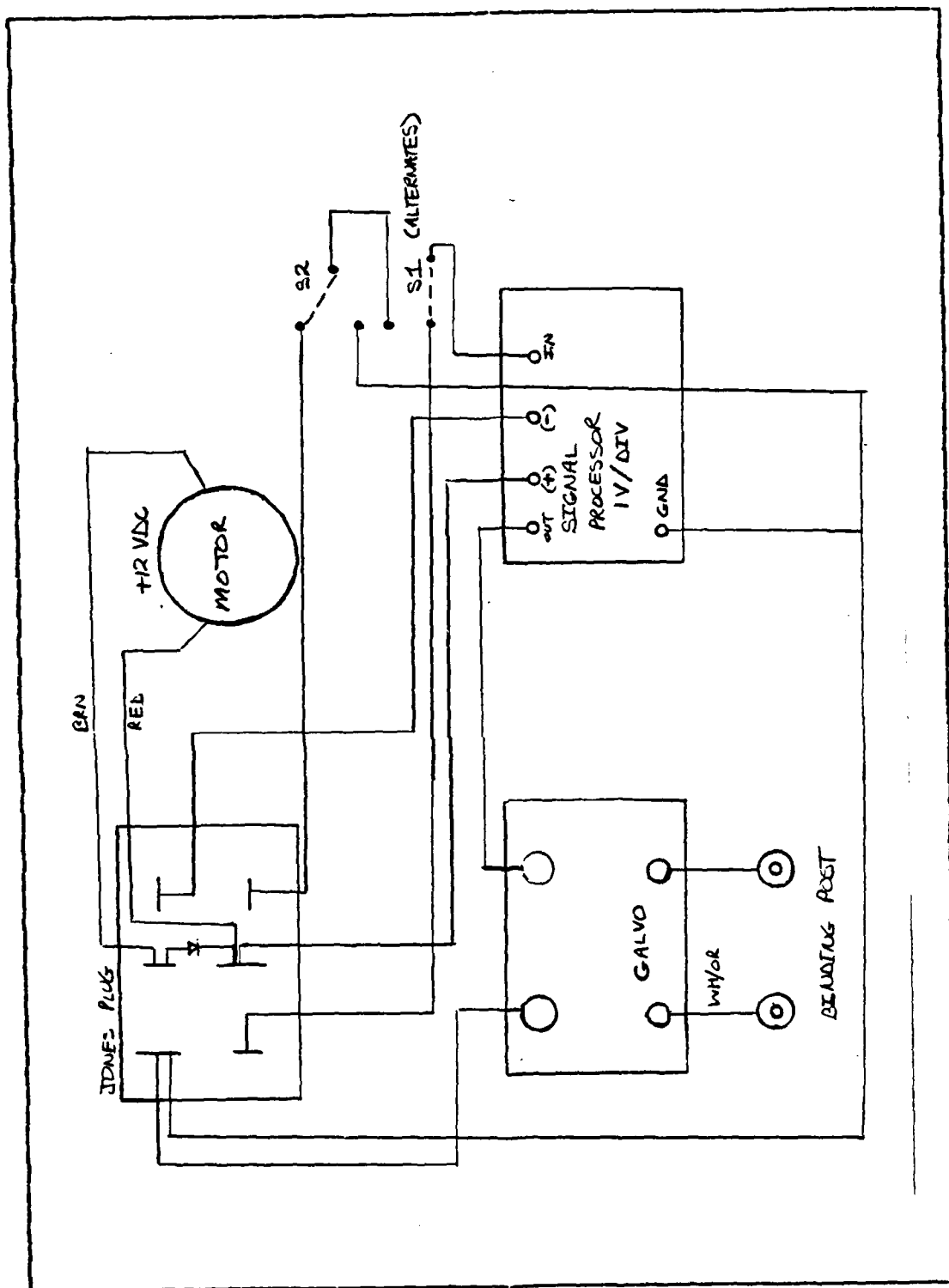
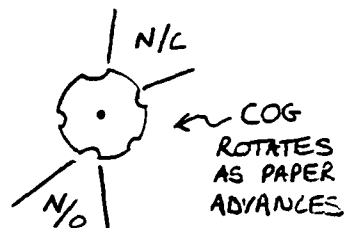
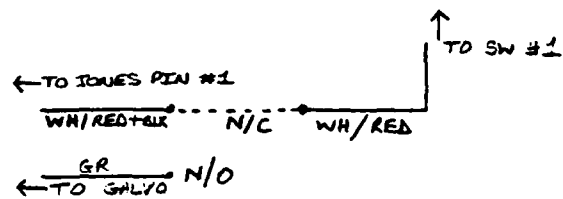


Figure 4.7 Rustrak Model 2146 with Signal Processor Schematic

UNMODIFIED SWITCH



MODIFIED SWITCH

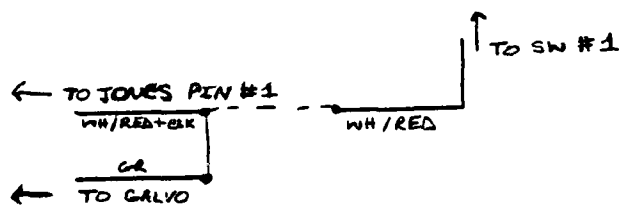


Figure 4.8 Single Channel Modification (S-MOD)

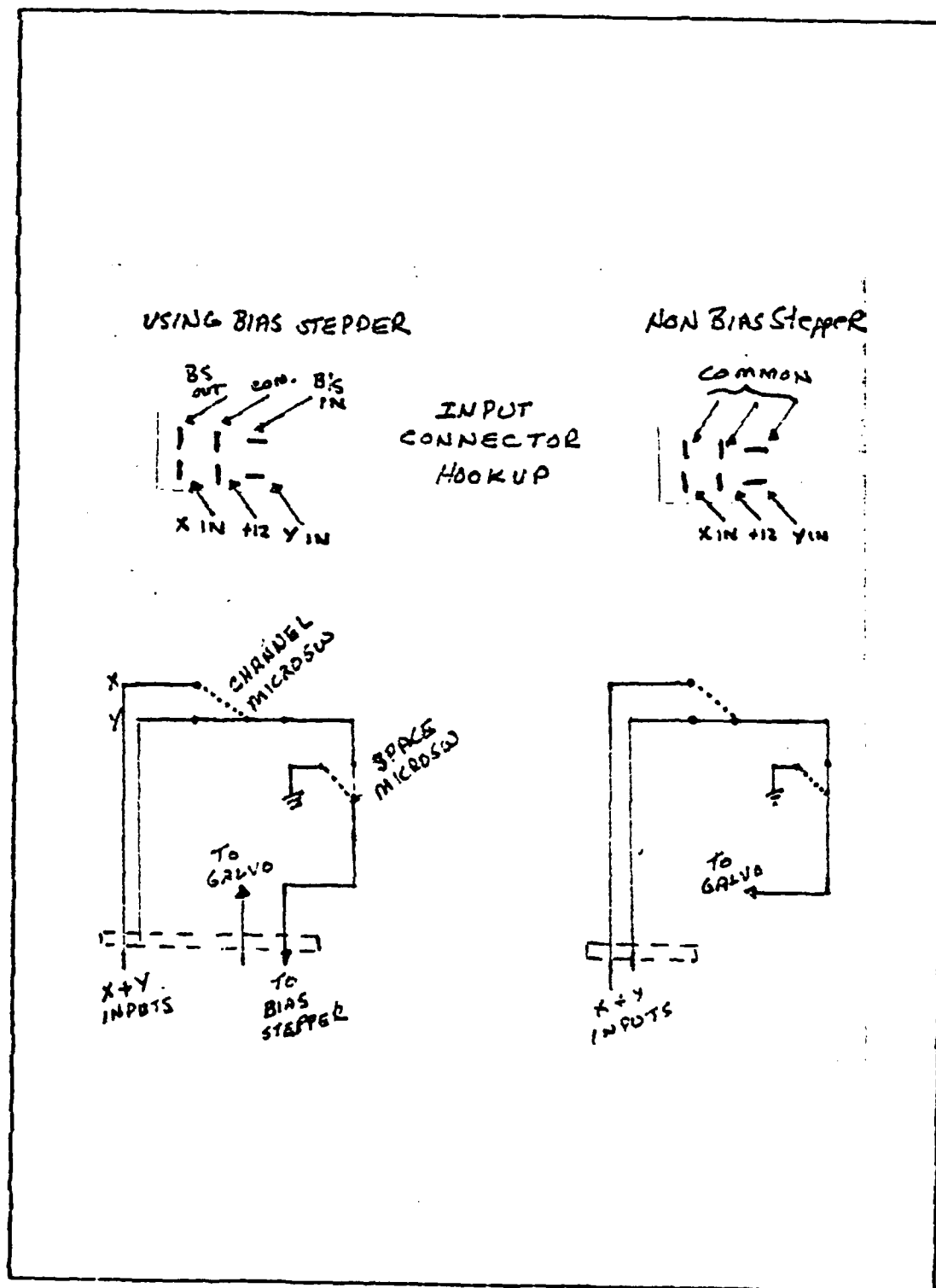


Figure 4.9 Bias Stepper Demodification

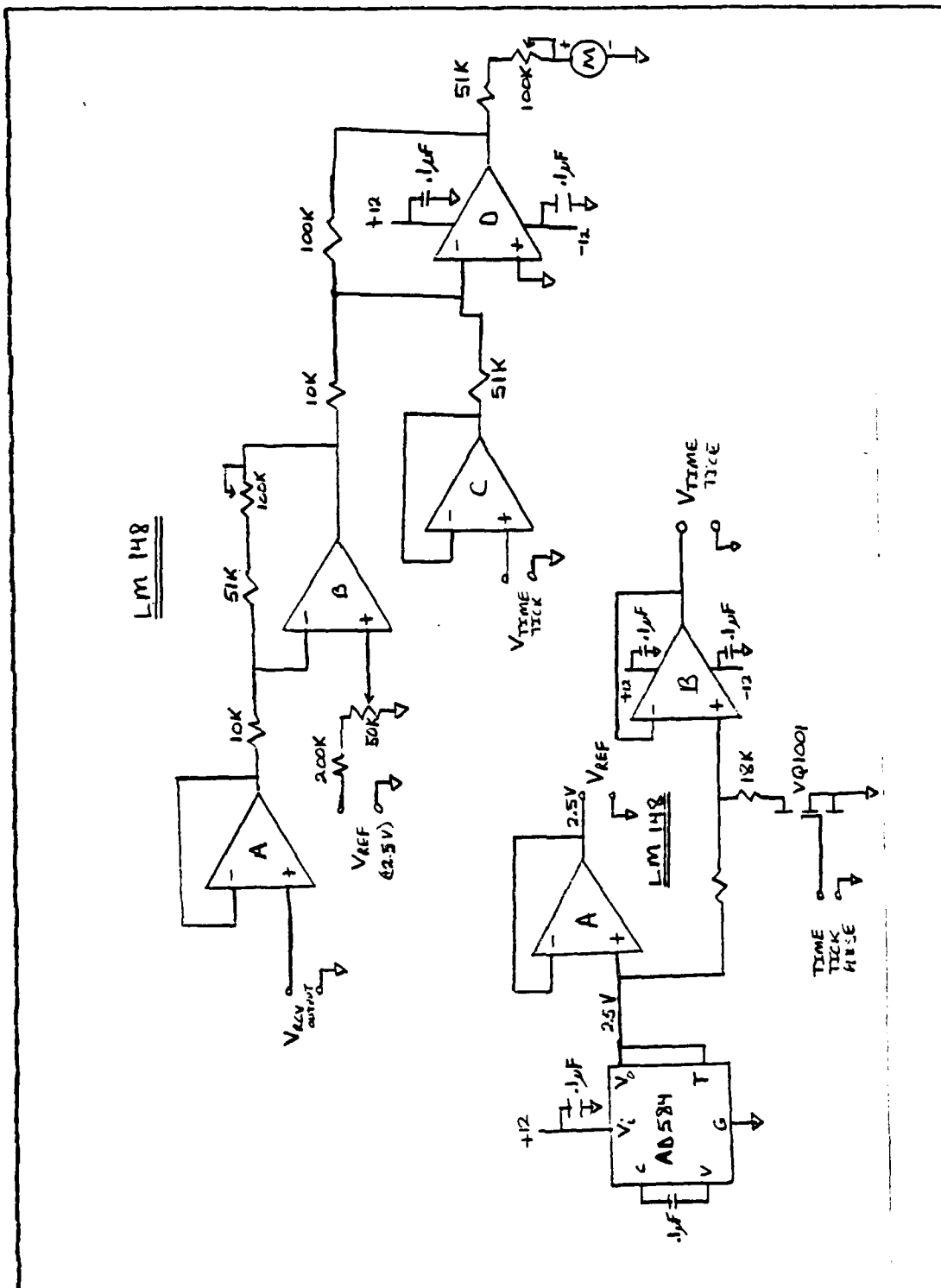


Figure 4.10 Interface Amplifier with Voltage Generator

indicated on the chart paper. Because of a requirement for ultra-low dissipation and operation using a battery source, a CMOS 21 stage counter timer (RCA CD4045A) was used in conjunction with CMOS 8 stage presettable synchronous down counters (RCA CD40103B) and a CMOS dual J-K master-slave flip-flop (RCA CD4027B) to obtain the time. The 2.097152 MHz crystal establishes the one second clock pulse as shown in Figure 4.11 . The time and the length of the pulse duration are set using 8-bit down counters. When the timer pulses, the length of the pulse indicates the time. A fifteen minute pulse will last for six seconds. A one hour pulse will last for twelve seconds and a twenty-four hour pulse will last for eighteen seconds. Time can be initialized as necessary by the reset switch.

V. PERFORMANCE OF SYSTEM

The informational parameter of a possible seismic event is variations in the level of the electromagnetic radiation envelope or in the number of radiation impulses whose amplitude exceeds a pre-chosen discrimination threshold. The noise measurement system is designed with a sensitivity range of 0.1 uV to 100 uV RF input. The system was given a "shakedown test" on the roof of Spanagel Hall at the Naval Postgraduate School to see if it was sensitive to variations in the level of electromagnetic radiation based on a 24 hour period.

Along the San Andreas Fault, it is expected that variations in signal level will occur due to seasonal changes. For instance, during autumn and winter the highest signal level falls into the sunless part of the day. Spring, summer, and the beginning of autumn have two maxima during the 24 hour period, the nightly and the post-noon ones. Figures 5.1, 5.2, 5.3, 5.4, and 5.5 are recordings which show the noise levels over a 24 hour period.

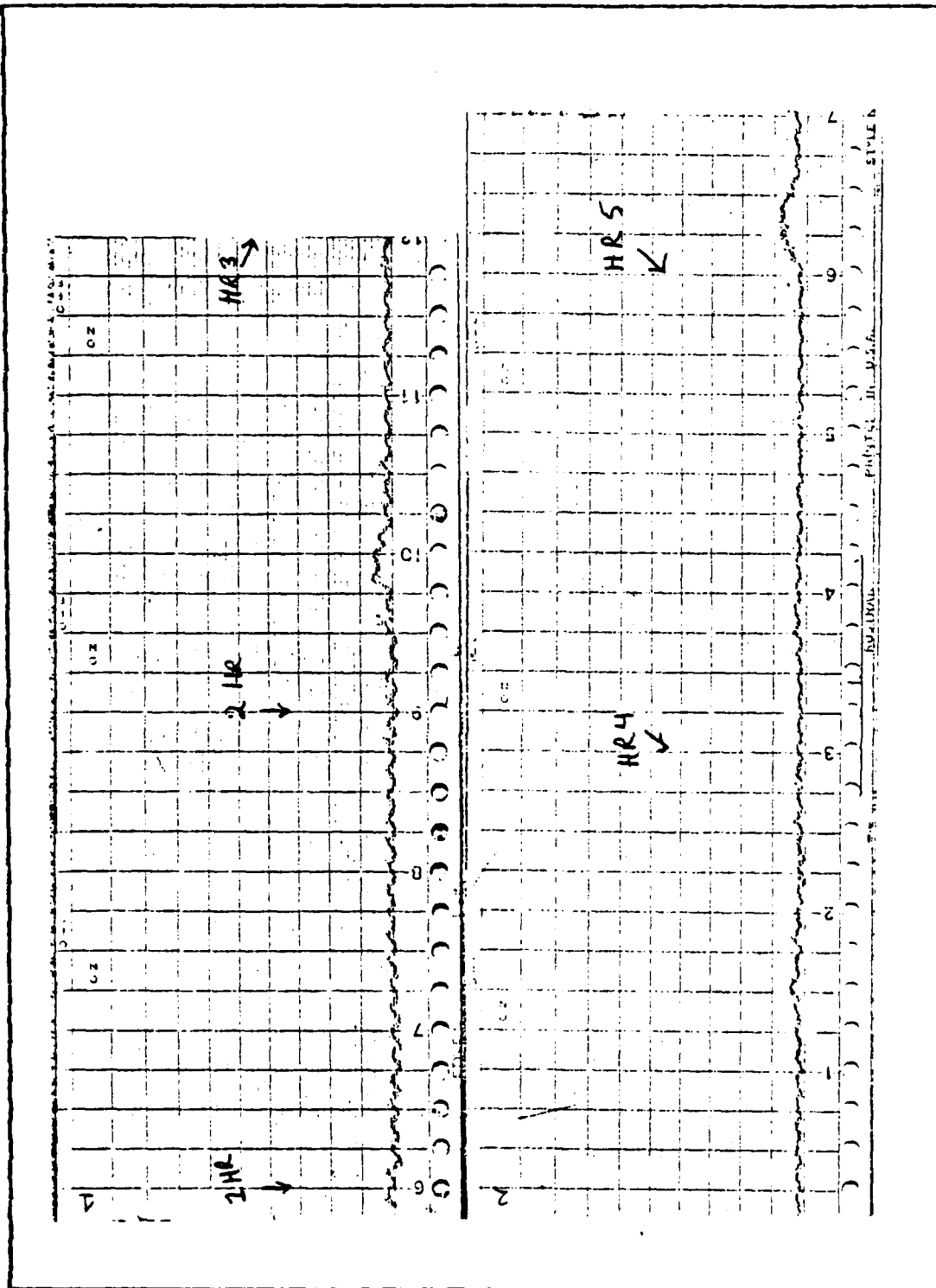


Figure 5.1 Signal Level Data from Noise Measurement System

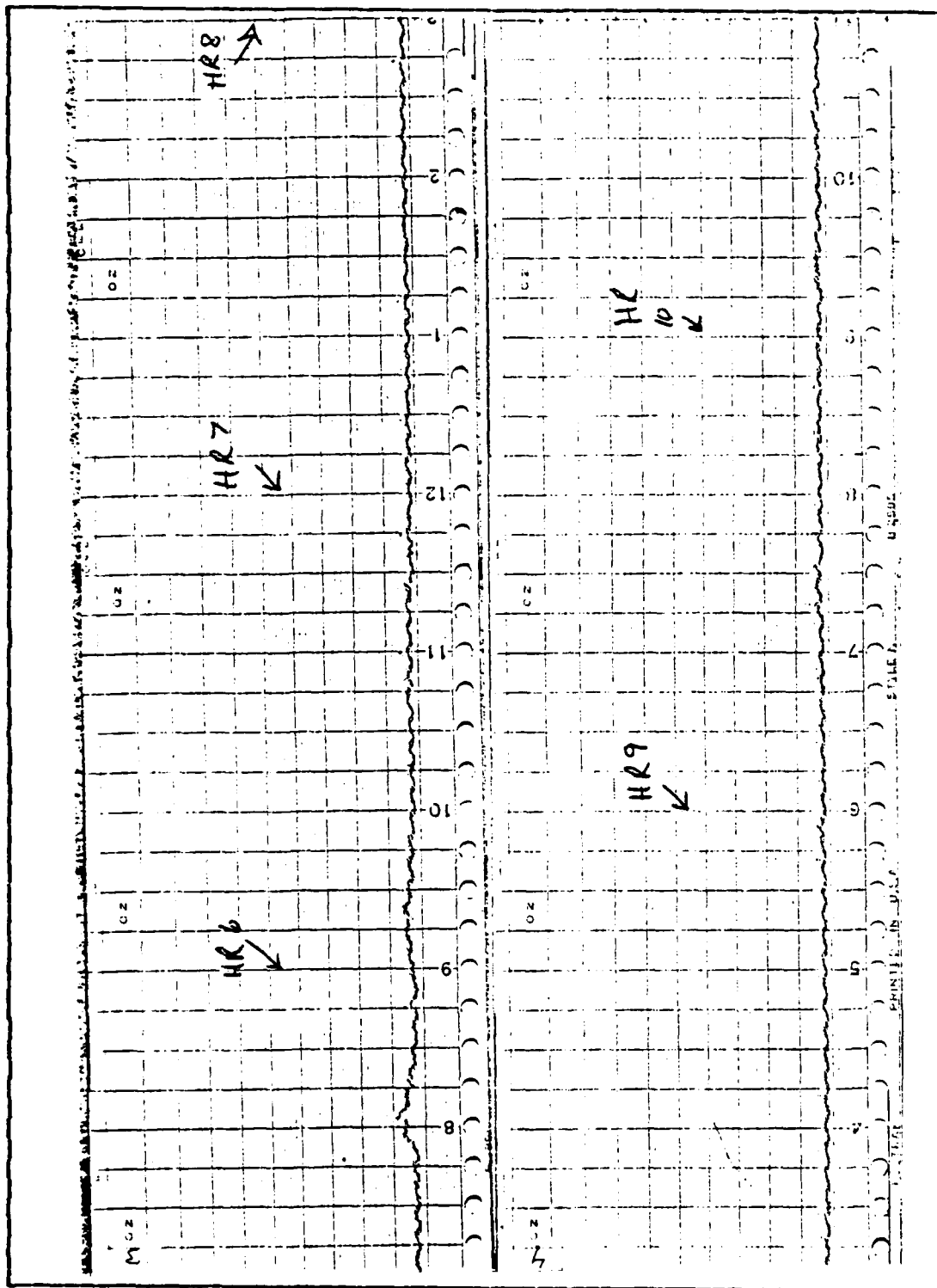


Figure 5.2 Signal Level Data from Noise Measurement System

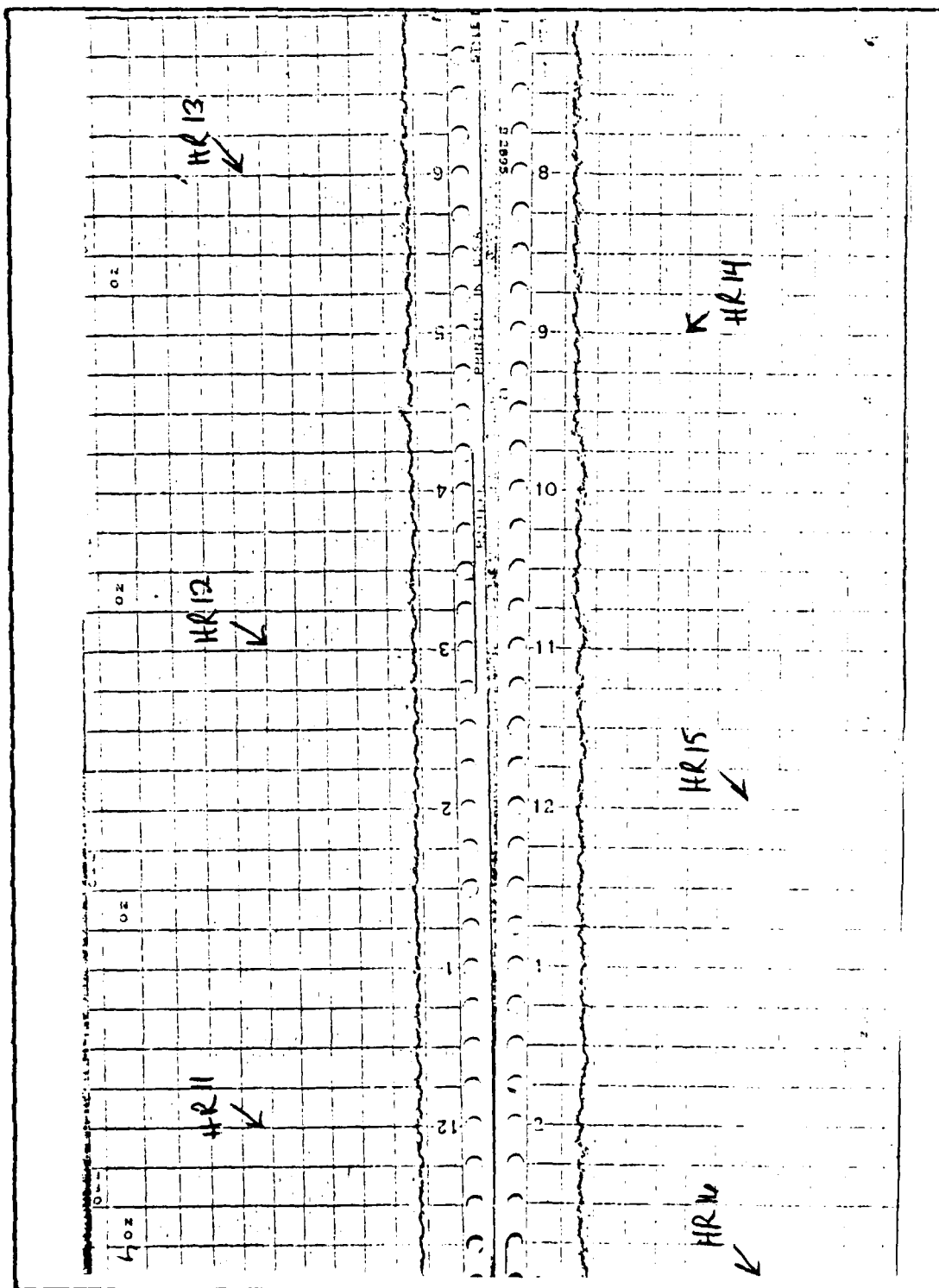


Figure 5.3 Signal Level Data from Noise Measurement System

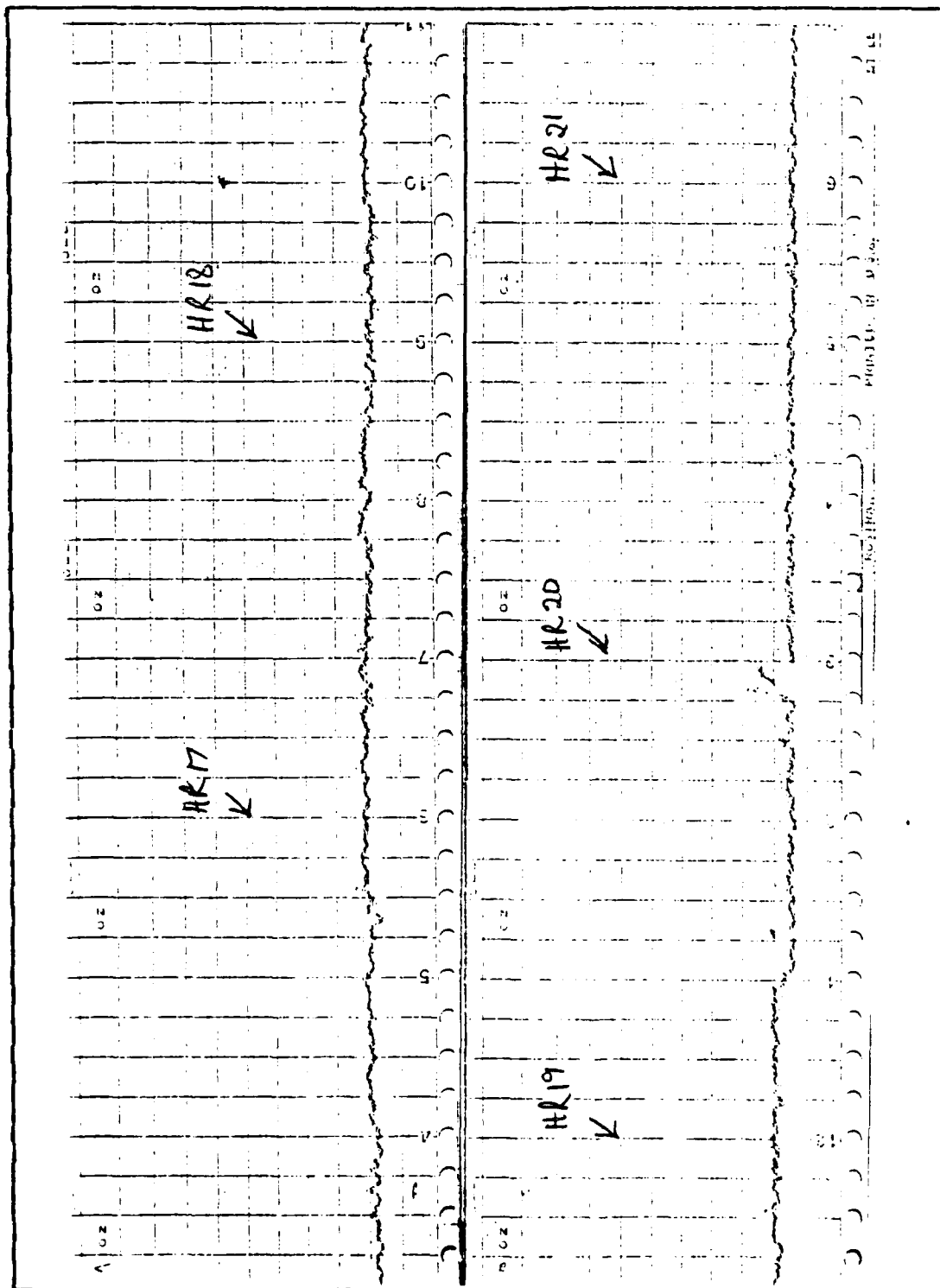


Figure 5.4 Signal Level Data from Noise Measurement System

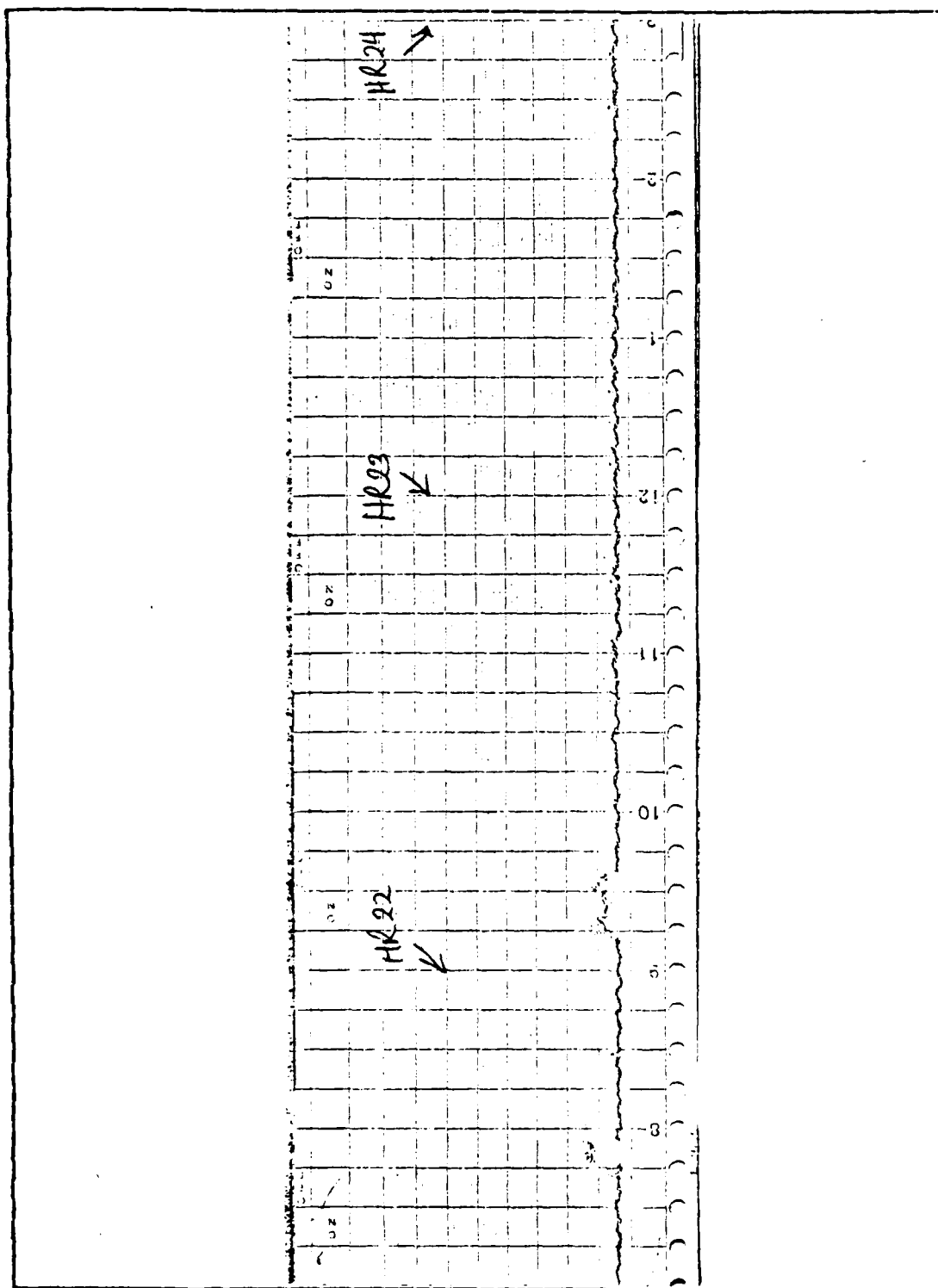


Figure 5.5 Signal Level Data from Noise Measurement System

INITIAL DISTRIBUTION LIST

	No.	Copies
1. Superintendent Attn: Library, Code 0142 Naval Postgraduate School Monterey, California 93943		2
2. Dr. Richard W. Adler Code 62 Naval Postgraduate School Monterey, California 93943		6
3. Dr. Stephen Jauregui, Jr. Code 62JA Naval Postgraduate School Monterey, California 93943		1
4. Defense Technical Information Center Cameron Station Alexandria, Virginia 22314		2
5. LT Mickey V. Ross 12 Ross Circle North Little Rock, Arkansas 72114		2
6. CAPT Carl Mortensen MS 977 U. S. Geological Survey 345 Middlefield Menlo Park, California 94025		2

12. Bleaney, B.I., and Bleaney, B., Electricity and Magnetism, p. 675, Oxford, London, 1957.
13. Johnston, M., Smith, B.E., and Mueller, R., "Tectono-magnetic Experiments and Observations in Western U.S.A.," Geomag. Geoelec. pp. 28, 85-97 1976.
14. Drickamer, H.F., and Frank, C.W., Electronic Transitions and the High Pressure Chemistry and Physics of Solids, Chapman and Hall, London, 1973.
15. Burke, J.J., Shock Waves and the Mechanical Properties of Solids, Syracuse Univ. Press, 1971.
16. Allen, F.E., "Shock Induced Polarization in Plastics," Journal of Applied Physics, Vol. 36, No. 7, p. 2111, 1965.
17. Kraus, J.D., and Carver, K.R., Electromagnetics, McGraw Hill, p. 402, 1973.
18. Los Alamos National Laboratory Technical Report 83-3120, Observations of an Ionospheric Perturbation Arising from the Coalinga Earthquake of 2 May 1983, by J.H. Wolcott, and D.J. Simons, 1983.

LIST OF REFERENCES

1. Friedlander, G.D., "Earthquake Prediction: A New Art," Spectrum, IEEE, pp. 46-57, September 1973.
2. Gokhberg, M.B., Morgounov, V.A., Yoshino, T., and Tomizawa, I., "Experimental Measurement of Electromagnetic Emissions Possibly Related to Earthquakes in Japan," Journal of Geophysical Research, Vol. 87, No. B9, Pages 7824-7828, 10 September 1982.
3. Derr, J.S., "Earthquake Lights: A Review of Observations and Present Theories," Bull. Seismological Society of America, Vol. 63, pp. 2177-2187, 1973.
4. Warwick, J., Stoker, C., and Meyer, T., "Radio Emission Associated With Rock Fracture: Possible Application to the Great Chilean Earthquake of May 22, 1960," Journal of Geophysical Research, Vol. 87, No. B4, April 1982.
5. Boore, D.M., "The Motion of the Ground in Earthquakes," Scientific American, Vol. 237, No. 6, pp. 68-78, 1977.
6. Dickinson, W.R., and Grantz, A., ed., Proceedings of Conference on Geologic Problems of San Andreas Fault System, Stanford Univ. Publication, Vol. 11, 1968.
7. Hauver, G.E., "Shock-Induced Polarization in Plastics. II. Experimental Study of Plexiglas and Polystyrene," Journal of Applied Physics, Vol. 36, No. 7, July 1965.
8. Schnurmann, R., and Warlow-Davies, E., "The Electrostatic Component of the Force of Sliding Friction," Proceedings, Physical Society of London, Vol. 54, September 1941.
9. Nitsan, U., "Electromagnetic Emission Accompanying Fracture of Quartz-Bearing Rocks," Geophysical Research Letters, Vol. 4, No. 8, August 1977.
10. Mizutani, H., Ishido, T., Yokokura, T., and Ohnishi, S., "Electrokinetic Phenomena Associated With Earthquakes," Geophysical Research Letters, Vol. 3, No. 7, July 1976.
11. Gokhberg, M.B., Gufeld, I.L., and Dobrovolsky, I.P., "Sources of Electromagnetic Earthquake Precursors," Academy of Sciences of the USSR, Schmidt Institute of Physics of the Earth, Vol. 250, No. 2, 1980.

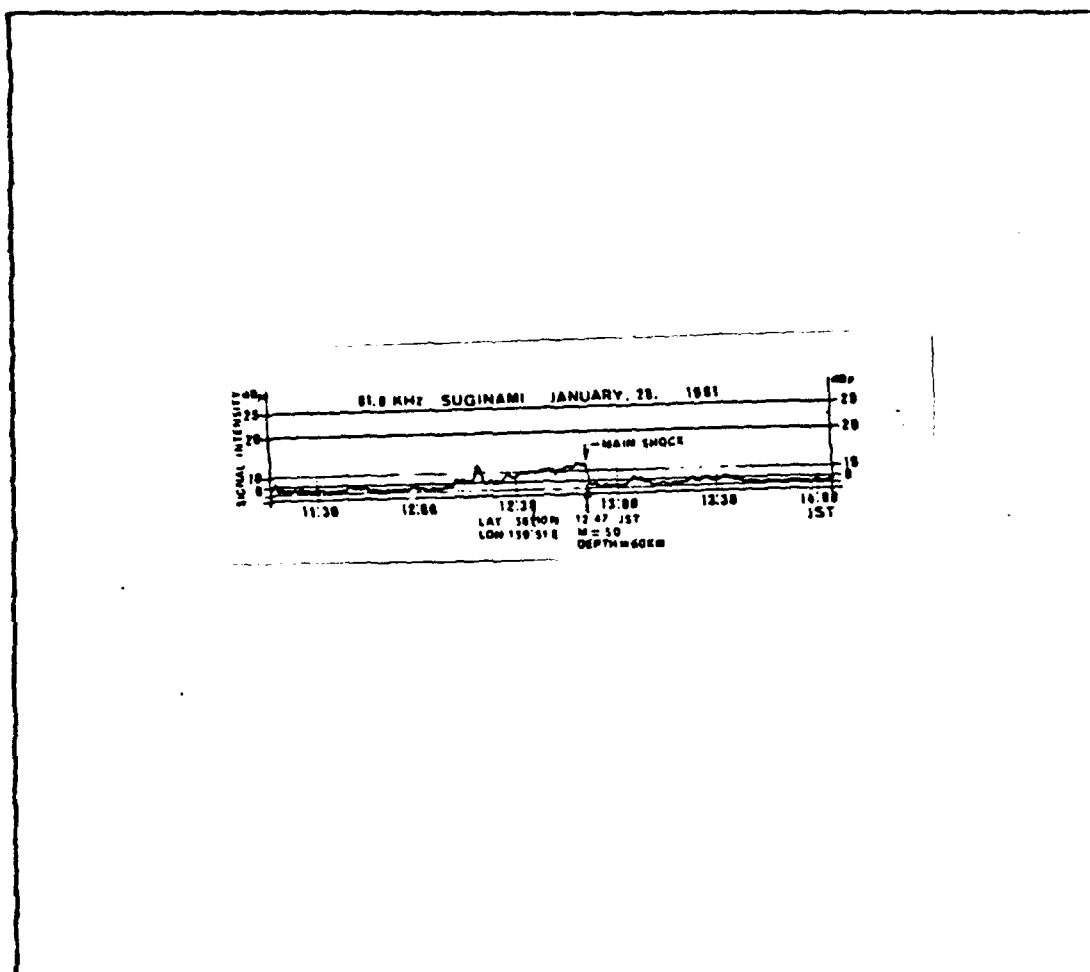


Figure B.5 Electromagnetic Noise Levels at Suginami

the observation point was approximately 50 Km. The depth of focus was 60 Km and the magnitude was 5.0. The noise level at 81 KHz increased to about 12 dB above the threshold level about 45 minutes before the main shock. Such a feature is quite similar to the typical events presented in Figure B.4.

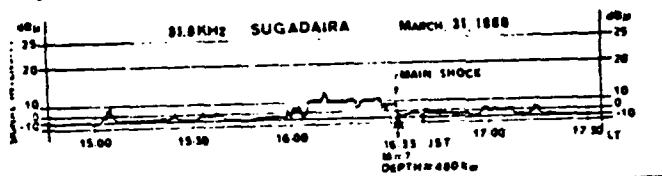


Figure B.4 Electromagnetic Noise Levels at Sugadaira

anomalous increase in the intensity. The amplitude exceeded the normal level by more than 15 dB. The normal level was approximately 8 μ V. It can also be seen in Figure B.4 that the intensity dropped sharply back to the previous level exactly at the moment of the shock.

Another event occurred at 1247 JST on January 28, 1981, as shown in Figure B.5 [Ref. 2]. The location of the epicenter was in the western Ibaragi prefecture on the northeastern side of Tokyo, and the distance between the epicenter and

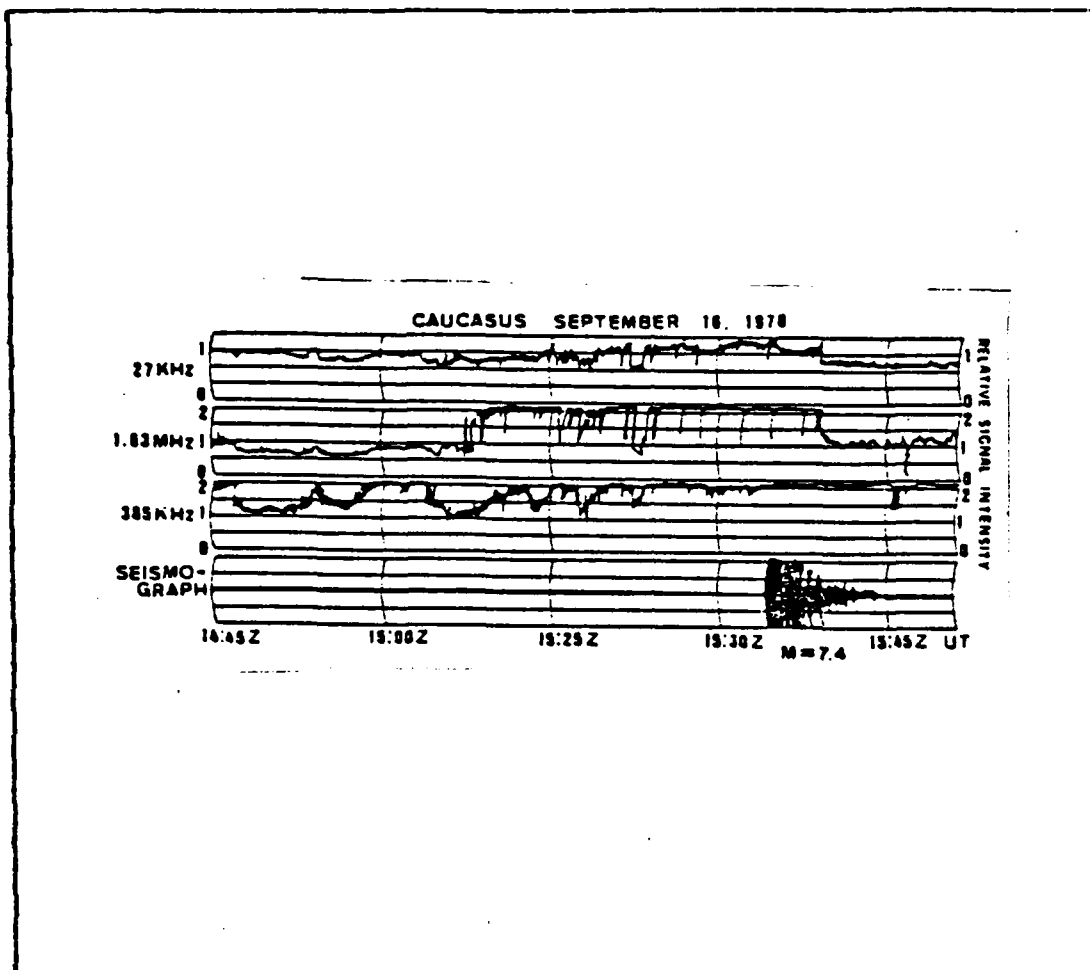


Figure B.3 Electromagnetic Noise Levels at Caucasus

C. JAPAN

On March 31, 1980, an earthquake occurred at 1633 Japan Standard Time (JST). The magnitude was 7, and the epicenter was located at 35.4° N and 135.3° E in the Kyoto prefecture. The focus of this earthquake was very deep, at approximately 480 Km. The distance between the location of the station and epicenter was around 250 Km.

As shown in Figure B.4 [Ref. 2], about half an hour before the shock, the 81 KHz data reception system recorded an

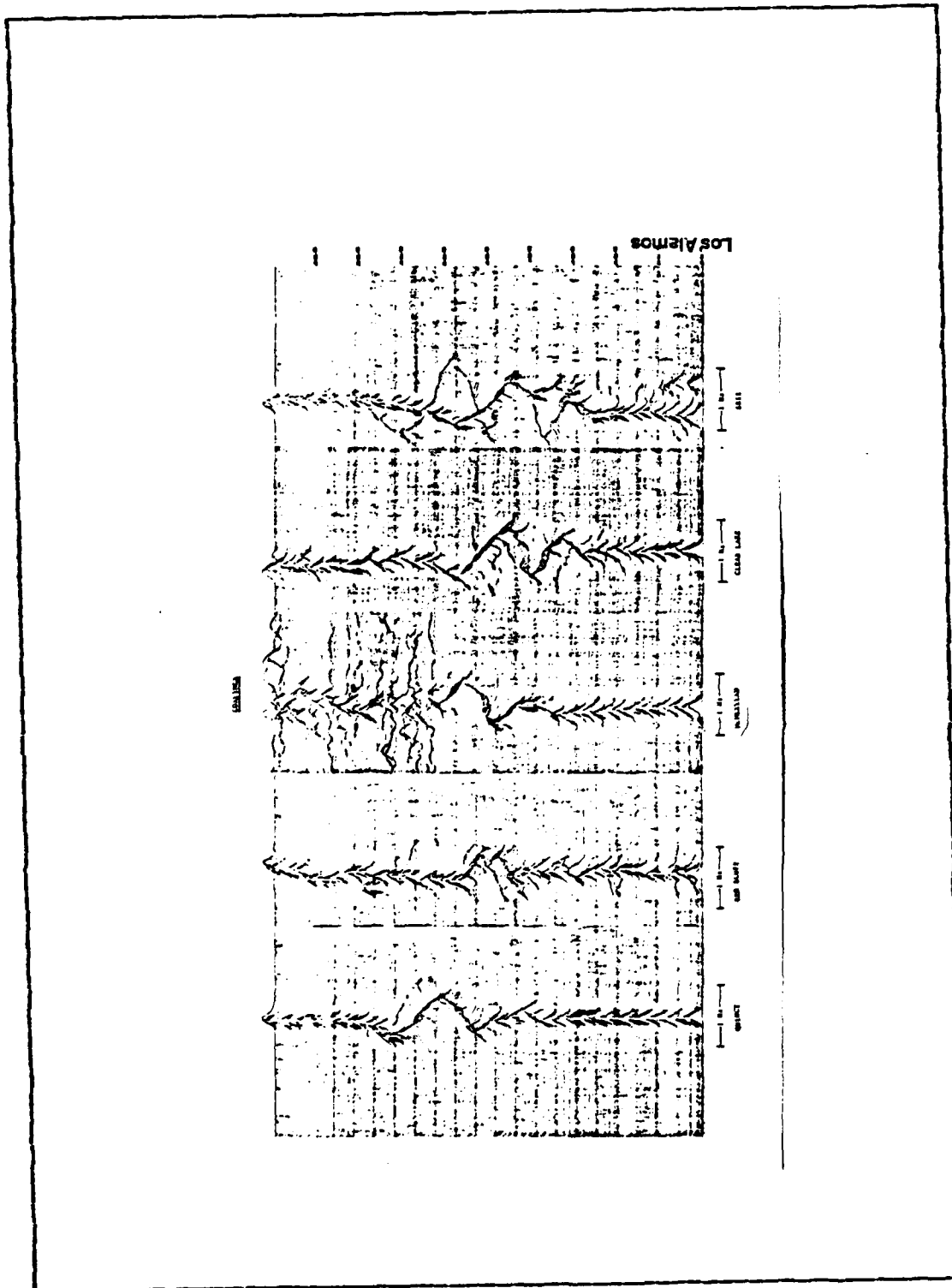


Figure B.2 Pseudo 3-D Plot of Doppler Disturbance Path

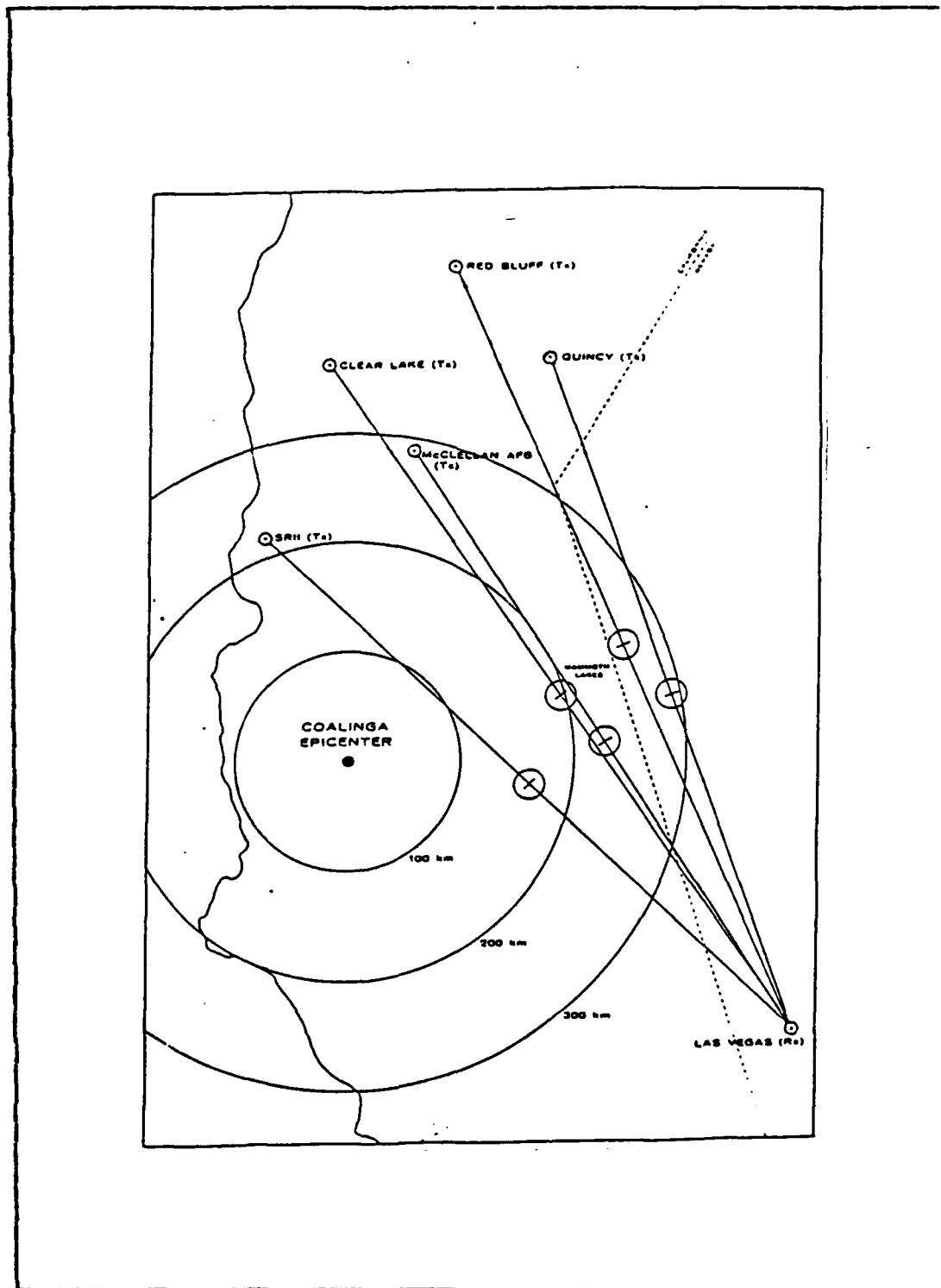


Figure B.1 Earthquake Epicenter and HF Path Locations

APPENDIX B
ELECTROMAGNETIC EMISSIONS FROM EARTHQUAKES

A. COALINGA

An ionospheric perturbation that was produced by the Coalinga earthquake of 2 May, 1983, was detected by a network of high frequency radio links in northern California. The ionospheric refraction regions of all five HF propagation paths, at distances between 160 and 285 km (horizontal range) from the epicenter, as shown in Figure B.1, were all affected by a ground-motion-induced acoustic pulse, as shown in Figure B.2, that propagated to ionospheric heights. These observations appear to be the first ionospheric disturbances to be reported this close to an earthquake epicenter [Ref. 18].

B. RUSSIA

Figure B.3 illustrates one example of the anomalous increase in electromagnetic radiation possibly related to earthquake activity on September 16, 1978. In this case, the epicenter of earthquake was located in central Iran, and the receiving equipment was set up in a tunnel 50 m below the ground surface at Caucasus, USSR, 1200 Km distant. The on-set time of electromagnetic radiation at frequencies of 27 KHz and 1.63 MHz was about 30 minutes before the main shock with magnitude of 7.4, as shown in Figure B.3 [Ref. 2].

TABLE V
Frequency 150.75 MHz
RF Input in μ V and Signal Output in mV

RF IN	S OUT	RF IN	S OUT	RF IN	S OUT	RF IN	S OUT
0.0	0.29	1.8	0.296	30	0.322	300	0.342
0.1	0.226	2.0	0.298	40	0.324	350	0.344
0.2	0.237	2.5	0.304	50	0.326	400	0.345
0.3	0.246	3.0	0.307	60	0.327	450	0.346
0.4	0.255	3.5	0.310	70	0.329	500	0.347
0.5	0.263	4.0	0.311	80	0.330	600	0.348
0.6	0.269	4.5	0.312	90	0.322	700	0.349
0.7	0.274	5.0	0.313	100	0.322	800	0.350
0.8	0.279	6.0	0.314	120	0.334	900	0.351
0.9	0.280	7.0	0.315	140	0.335	1.0 mV	0.352
1.0	0.284	8.0	0.315	160	0.336	1.4 mV	0.355
1.2	0.287	9.0	0.316	180	0.337	1.6 mV	0.355
1.4	0.290	10	0.317	200	0.338	2.0 mV	0.356
1.6	0.293	20	0.319	250	0.340	MAX	0.358

TABLE IV
Frequency 38.45 MHz
RF Input in μ V and Signal Output in mV

RF IN	S OUT	RF IN	S OUT	RF IN	S OUT	RF IN	S OUT
0.0	0.268	1.8	0.227	30	0.306	300	0.327
0.1	0.220	2.0	0.228	40	0.311	350	0.328
0.2	0.220	2.5	0.233	50	0.315	400	0.329
0.3	0.220	3.0	0.237	60	0.317	450	0.330
0.4	0.221	3.5	0.241	70	0.318	500	0.331
0.5	0.221	4.0	0.246	80	0.319	600	0.332
0.6	0.221	4.5	0.249	90	0.320	700	0.333
0.7	0.221	5.0	0.253	100	0.320	800	0.333
0.8	0.221	6.0	0.262	120	0.321	900	0.333
0.9	0.221	7.0	0.267	140	0.321	1.0 mV	0.334
1.0	0.222	8.0	0.271	160	0.322	1.4 mV	0.334
1.2	0.223	9.0	0.275	180	0.323	1.6 mV	0.334
1.4	0.224	10	0.279	200	0.323	2.0 mV	0.334
1.6	0.225	20	0.296	250	0.326	MAX	0.335

APPENDIX A
RECEIVER SENSITIVITY DATA AT VHF FREQUENCIES

B. RECOMMENDATIONS

Data acquired from the VHF noise measurement system should be taken for at least a year observing background noise level variations. Since seismological data can be acquired from the Geological Survey Office, any significant earthquake in the area of the noise measurement site should be immediately compared with the recorded data. Otherwise data can be examined on a periodic basis.

Although several studies were presented concerning the mechanism by which rocks emit radiowave energy when they are crushed, further investigation is needed in this area and the following:

1. The relation between the intensity of the background noise in the VHF range and the location of the epicenter. The antennas of the noise measurement system are looking up and down the fault which makes location probable.
2. The relation between the intensity of the precursor VHF radio noise and the earthquake's magnitude and depth of focus. The data obtained may show similar variations in background noise levels at 38 MHz or 150 MHz or both for earthquakes of similar magnitude and depth of focus.
3. Long term data collection is needed to obtain through order-of-magnitude calculations, the amount of VHF radio noise radiated in these events.

VI. CONCLUSIONS AND RECOMMENDATIONS

A. CONCLUSIONS

The design, construction, and testing of an RF noise measurement and recording system in the 30 MHz and 150 MHz range has been described. Test results show that background noise levels can be received and recorded from tenths of microvolts to volts. Theory has shown that anomalous electromagnetic radiation levels from earthquakes can occur. The noise measurement system data will not only detect the presence of increased background noise levels at the designated frequencies, but it may also give an indication of the direction of reception relative to the San Andreas Fault due to the polarization of the antennas.

Besides physically erecting the antennas along the fault, the most difficult problem was designing a receiver/recorder system that would be sensitive to slight changes in background noise level at frequencies near those of citizen band and amateur radio operators. The signal output of the receiver was sent through an interface amplifier and the chart recorders modified to accomplish this.

Appendix B presents electromagnetic emissions and other observations possibly related to earthquake precursor activity. Measurements of electromagnetic radiation from earthquakes were detected by changes in background noise levels, but in the very low, low, and high frequency ranges. The results of this research suggest that electromagnetic radiation measurements has potential as an earthquake prediction tool.

END

FILMED

7-85

DTIC